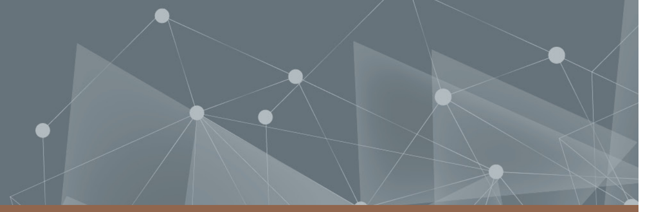

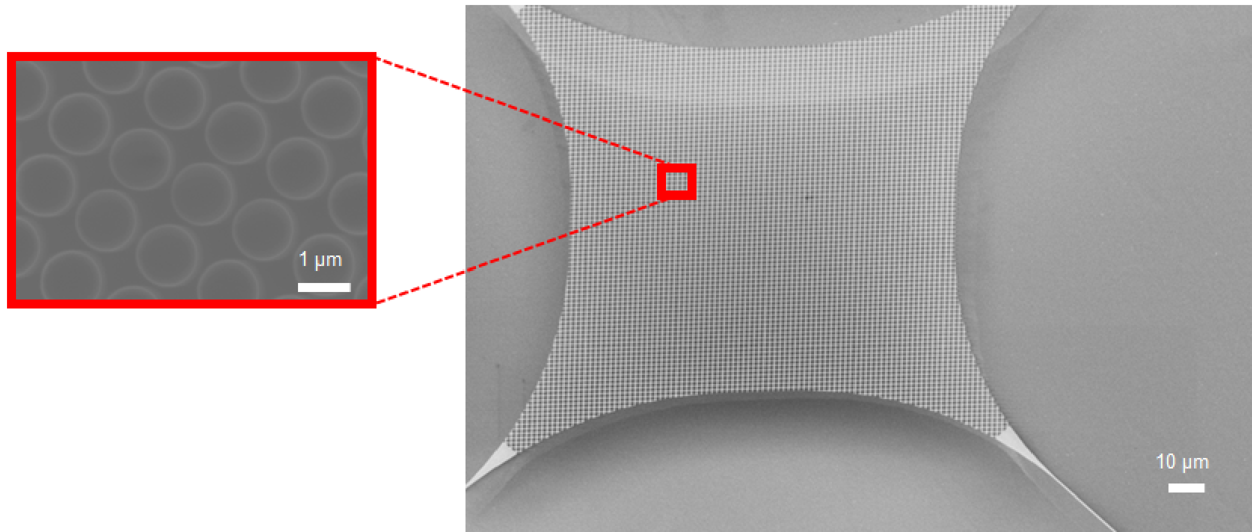

Tensile-strained micromechanical resonators made from crystalline InGaP with low mechanical dissipation and high optical reflectivity

Master's Thesis in Nanoscience and Nanotechnology

FIA HELLMAN

Department of Microtechnology and Nanoscience
CHALMERS UNIVERSITY OF TECHNOLOGY
Gothenburg, Sweden 2022
www.chalmers.se

Master's thesis 2022

Tensile-strained micromechanical resonators made from crystalline InGaP with low mechanical dissipation and high optical reflectivity

FIA HELLMAN

CHALMERS
UNIVERSITY OF TECHNOLOGY

Department of Microtechnology and Nanoscience
Division of Quantum Technology Laboratory
Chalmers University of Technology
Gothenburg, Sweden 2022

Tensile-strained micromechanical
resonators made from crystalline InGaP
with low mechanical dissipation
and high optical reflectivity
FIA HELLMAN

© FIA HELLMAN, 2022.

Supervisors: Sushanth Kini and Anastasiia Ciers, Department of Microtechnology and Nanoscience
Examiner: Witlef Wieczorek, Department of Microtechnology and Nanoscience

Master's Thesis 2022
Department of Microtechnology and Nanoscience
Chalmers University of Technology
SE-412 96 Gothenburg
Telephone +46 31 772 1000

Cover: A trampoline-shaped micromechanical resonator with photonic crystal fabricated during this thesis.

Typeset in LaTeX
Printed by Chalmers Reproservice
Gothenburg, Sweden 2022

FIA HELLMAN
Department of Microtechnology and Nanoscience
Chalmers University of Technology

Abstract

The interest in micro- and nanomechanical resonators has grown rapidly during the last decade due to their broad applicability within metrology and fundamental science. They have, for instance, been brought to the quantum regime and have also been demonstrated to be incredibly precise detectors of small masses, forces, or displacements. A micromechanical resonator's motion can be detected via optical means, where the resonator's reflectivity enhances the coupling between it and the light —– resulting in a more efficient read-out. High-reflectivity micromechanical resonators can be achieved by alternating their in-plane dielectric constants with structures known as photonic crystals. On the other hand, a precise read-out of the resonator's displacement requires low mechanical dissipation for the measurement signal to exceed the thermal noise floor. Dissipation can be minimized by carefully selecting the appropriate material, design, and operating environment for the resonator. Furthermore, mechanical dissipation can even be diluted by introducing tensile strain to the material, which acts as additional storage of energy. The quality factor, which is the ratio between the total energy stored in the system and energy lost during one cycle, is commonly used to quantify mechanical dissipation.

This thesis uses highly tensile strained crystalline InGaP to realize micromechanical resonators with low mechanical dissipation. Crystalline materials are promising candidates for highly sensitive micromechanical resonators due to their potentially low intrinsic dissipation, high intrinsic strain, and yield strength. The first part of this thesis investigates the first two of these properties for InGaP by comparing fabricated doubly-clamped strings with analytical models. It was inferred that the stress depends on the crystal direction and varies between 200-500 MPa. Further, the InGaP used in this thesis shows an intrinsic quality factor between 5700 ± 1000 up to 7900 ± 1700. The second part of this thesis focuses on optimizing the geometry of trampoline-shaped micromechanical resonators to enhance their mechanical quality factor and their optical reflectivity. An improved optical reflectivity was observed for fabricated devices patterned with a photonic crystal. FEM-based simulations were made to find dimensions of the trampoline that considerably reduce mechanical clamping loss to the surrounding supporting structure. Implementing these designs to trampoline-shaped micromechanical resonators showed a quality factor of $7 \cdot 10^6$ at low temperatures, which was not limited by clamping loss. It was instead demonstrated that the quality factor was limited by gas damping. The mechanical and optical properties of micromechanical resonators fabricated from crystalline InGaP demonstrated in this thesis have shown promising results and provide all requirements for the resonators to be used in optomechanical systems in the near future.

Acknowledgements

This thesis would not have been possible to make without the enormous help from my supervisors: Sushanth Kini, Anastasiia Ciers, and Associate Prof. Witlef Wieczorek. Thanks to all of you for your patience and the time you have sacrificed to help me with my work.

Witlef, thank you for the opportunity to do this thesis and be a part of the optomechanical team. Also, thank you for all the feedback and support. From all this feedback, I have gained more knowledge about this area of research. You have also helped me improve my way of presenting my thoughts and work in a better way. Anastasiia, even if I didn't get to have too much time with you until you left for maternity leave, you still gave me a lot. For instance, you helped me understand how many concepts within this research area were connected. Now to you, Sushanth. Thank you for all the time you sacrificed to help me with everything from simulations to characterization. You have always done this with a calm and positive spirit, which I appreciate and will never forget. I am pleased that I got the opportunity to work with all of you. Also, I would like to thank my remaining colleagues: Hanlin, Martí, Avan, and Achintya, for always being there and helping me when I had questions.

Lastly, I want to thank my inspirations and those closest to me. First, I want to thank my friends, who always supported me. My heart and partner, Fredrik. You have helped me in many different areas. One of many is that you always helped me see things from an optimistic point of view. You have given me so much within the last few years, and I am happy to have you by my side. My bellowed sister Tessie, we have always been different and seen things from different perspectives. This has challenged me to think in new ways and made me who I am today. Mamma and Pappa, you have never expected anything from me but have always been happy for my success and supported my choices. This has allowed me to develop for my own sake while still feeling that you are by my side.

Fia Hellman, Gothenburg, September 2022

Contents

List of Acronyms **xi**

Nomenclature **xiii**

List of Figures **xvii**

List of Tables **xix**

1 Introduction **1**
1.1 Thesis organization 2

2 Theory **5**
2.1 Basic concept behind a mechanical resonator 5
2.1.1 Classical description 5
2.1.2 Quantum description 7
2.2 Sources of Mechanical Dissipation 8
2.2.1 Intrinsic dissipation 9
2.2.1.1 Thermoelastic dissipation 9
2.2.1.2 Dissipation through TLS 10
2.2.1.3 Surface losses 11
2.2.2 Extrinsic 11
2.2.2.1 Clamping losses 12
2.2.2.2 Gas damping 12
2.3 Engineer and minimize mechanical dissipation 13
2.3.1 Minimizing clamping loss 13
2.3.2 Strained resonators 14
2.3.2.1 Dissipation Dilution 16
2.3.3 Soft Clamping 18
2.3.4 Strain engineering 20
2.4 Optical read-out of mechanical motion 22
2.4.1 How the reflectivity of a mirror can be improved 22

3 Methods **25**
3.1 Simulations 26
3.1.1 FEM simulations of mechanical properties 26
3.1.2 Simulations of optical reflection 27
3.2 Fabrication 28

3.3 Characterization set-ups 29
3.3.1 Characterization of mechanical properties 29
3.3.1.1 Lorentzian fit 32
3.3.1.2 Ringdown 32
3.3.2 Characterization of optical reflectivity 33

4 Results **35**
4.1 1D resonators - Strings 35
4.1.1 Design of strings 35
4.1.2 Mechanical characterization of strings 36
4.2 Trampoline-type micromechanical resonators 40
4.2.1 Optimizing the design for trampolines to enhance mechanical Q 41
4.2.2 Mechanical characterization of trampolines 47
4.2.3 Design of PhC 51
4.2.4 Characterization of reflectivity for PhC 53

5 Conclusion **57**

Bibliography **59**

A Appendix **I**
A.1 Data for simulations I

List of Acronyms

The following is the list of acronyms that have been used throughout this thesis:

CPD	Critical Point Dryer
DIW	Deionised Water
EBL	Electron Beam Lithography
ICP-RIE	Inductively Coupled Plasma Reactive Ion Etch
IPA	Isopropanol
LO	Local Oscillator
NPS	Noise Power Spectrum
PBS	Polarizing Beam-Splitter
PhC	Photonic Crystal
PID	Proportional–Integral–Derivative controller
PM	Phase Modulator
PML	Perfectly Matched Layer
PnC	Phononic Crystal
SEM	Scanning Electron Microscopy

Nomenclature

Below is the nomenclature of parameters that have been used throughout this thesis.

Parameters

a	Lattice constant
A	Cross-sectional area
A_0	Initial amplitude
c	Constant fit parameter
C_p	Specific heat capacity
D_{Beam}	Diameter of beam
D_{Mirror}	Diameter of the mirror
E	Young's modulus
f	Resonance frequency
F	Force
h	Thickness of micromechanical resonator
$\hbar$	Reduced Planck constant
I	Geometrical moment of inertia
I_{i}	Intensity measured at i
k	Effective spring constant
k_{r}	Wave number
k_{B}	Boltzmann's constant
L	Length of a string shaped micromechanical resonator
L_{cl}	Clipping loss
m	Effective mass
n	Mode number

P	Pressure
$P(t)$	Power
q	Phonon
Q	Mechanical quality factor
R	Reflectivity
t	Time
T	Temperature of the thermal bath
u	Displacement field
$\|u\rangle$	Energy level
v	Acoustic velocity
V	Potential energy
V_i	Voltage measured at i
x	Position along x-axis
x_{zpf}	Zero point fluctuation
w	Width of a string shaped micromechanical resonator
$w(z)$	Beam size at a position z
w_0	Waist
w_{PML}	Width of PML
w_{buffer}	Distance between resonator and PML
W	Total amount of energy stored in a micromechanical resonator
z	Position along z-axis
z_0	Rayleigh range
α	Linear thermal expansion coefficient
$\alpha(t)$	Fluctuating amplitude of a light field
Γ	Decay rate
$\delta X(t)$	Amplitude quadrature
$\delta Y_{\mathrm{s}}(t)$	Phase quadrature
ΔW	Amount of energy that dissipated during one oscillation for a micromechanical resonator
θ	Azimuthal angle
κ	Thermal conductivity
λ	Wavelength

λ_{PML}	the wavelength of the acoustic wave
ν	Poisson ratio
ϵ	Dielectric constant
ϵ^{II}	In-plain strain
ρ	Mass density
σ	Tensile stress
ϕ	Polar angle
Φ	Phase
$\Phi(x)$	Mode shape
χ	Susceptibility
ω	Angular frequency
ω_{m}	Angular resonance frequency

Parameters for different materials

Parameters	$In_{0.42}Ga_{0.58}P$ [1]	GaAs [2]	Si_3N_4 [3]	Si [2]	SiC [2]
$\alpha * 10^{-6}$ [1/K]	4.6	5.6	3.7	2.6	3.0
E [GPa]	85 - 130	120	200	170	420
C_p [J/kgK]	380	550	1100	710	940
ρ [kg/m^3]	4400	5300	3250	2330	3200
κ [W/mK]	66	45	43	150	70
Yield strength [GPa]	—	3.0 [4]	6.4 [5]	8.3 [6]	21 [7]

Table 0.2: Parameters for different materials at 300 K.

List of Figures

1.1 SEM images of different geometries used in state-of-the-art micro-resonators. 2
1.2 Schematics illustration of the two kinds of resonators which are treated in this thesis. 3

2.1 Schematic illustration of a simple harmonic oscillator with effective mass m and effective spring constant k. 5
2.2 Illustration of the motion of an damped harmonic oscillator as a function of time, see Equation 2.5. 6
2.3 The thermal expansion coefficient α as a function of temperature for three different materials - GaP, InP and InGaP. 10
2.4 Schematic illustration of tunneling between two energy levels $|u\rangle$ and $|v\rangle$. 11
2.5 A PnC used to minimize clamping loss with a resonator (membrane) placed in the center of the PnC. Picture is taken from Ref. [38]. 14
2.6 A schematic picture of the origin of strain from lattice mismatch. Gray is the substrate and blue the device layer. Picture is taken from Ref. [27]. 15
2.7 The mode shape of a tensile strained string resonator of length L and its first and second derivative. 17
2.8 The influence soft clamping has on the mode shape and the bending ($u''(x)$) in a) and b), respectively. 19
2.9 Example of different resonators that implement soft clamping. 20
2.10 Resonators that uses strain engineering. 21
2.11 Illustration of PhC. 23
2.12 A SEM image of a PhC with a diameter of D_{Mirror} from the top together with a drawing of a beam with a diameter of D_{Beam}. 24

3.1 Schematic illustration of the wafer used in this thesis. 25
3.2 The different kinds of mesh are used in this thesis. 26
3.3 An illustration of the chip after each fabrication step. 28
3.4 Schematic illustration of the homodyne set-up used in this thesis. 31
3.5 Example of NPS from a homodyne measurement. 32
3.6 Example of a ringdown measurement 33
3.7 Schematic illustration of optic set-up to measure the reflectivity of PhC. 34

4.1 Design of strings. 36
4.2 Image of fabricated suspended strings. 37
4.3 Image of strings with different width oriented along [110 37
4.4 Measured frequency dependence of strings. 38
4.5 Extraction of stress from strings. 39
4.6 Measured Q for strings. 40
4.7 Extraction of Q_{int}. 40
4.8 Geometry of the trampoline resonators used for COMSOL simulations. 41
4.9 Orientation for trampoline in simulations. 42
4.10 Result of the quality factor and the fundamental frequency from simulations for different parameter-sweeps. 44
4.11 Investigation of clamping for different r_{out}. 45
4.12 The directions influence on $Q \cdot f$ for simulations. 46
4.13 First fabrication of optimized trampolines. 47
4.14 Optical images of the result from the second fabrication of optimized trampolines. 48
4.15 NPS for optimized trampolines with $w_t = 0.5\mu$m together with an insert of the COSMOL image of the fundamental mode and which peak it corresponds to. 49
4.16 w_t impact of the mechanical properties. 49
4.17 Pressure dependence of Q for the fundamental mode of a trampoline resonator and analytical model of Q_{gas} from Equation 4.17 50
4.18 Q measured at different temperatures. 51
4.19 Simulated reflectivity of PhC at $\lambda = 1550$ nm with respect to a_{PhC} and r_{PhC}. 52
4.20 Reflectivity dependence on wavelength. 52
4.21 Clipping loss for different D_{Mirror} with a waist of 7.4 μm 53
4.22 Optical and SEM images of devices with PhC with varying size of r_{PhC}. 53
4.23 Measured reflectivity of PhC. 54
4.24 Schematic illustration of a guided and cavity mode. 54
4.25 Comparison of reflectivity obtained from simulations and measurements. 55

List of Tables

0.2 Parameters for different materials at 300 K. xv

4.1 Reference values of the parameters for COMSOL simulations. 41
4.2 The parameters used for the first generation of fabricated trampolines. 47
4.3 The parameters used for the second generation of fabricated trampolines. 48

1 Introduction

The interest and implementation of micro- and nanomechanical resonators have grown rapidly during the last decade due to their many implementations within metrology and fundamental science. For instance, they have been cooled to their ground state, and thereby enabled investigation of the quantum behavior of mechanical systems. Furthermore, micromechanical resonators are good candidates for ultrasensitive sensors due to their small mass. These sensors can detect feeble forces, masses, displacements, radiation, and temperatures, only to name a few. For instance, it can be used in chemical, medicine, and biological research by enabling advances in mass spectrometry. Here, the resonator's resonance frequency shifts as a small mass, such as a molecule, is absorbed to its surface [8]–[10]. Even masses as small as zepto grams have been detected with nanomechanical resonators [11]. A signal must exceed the thermal force noise limit to be detected in classical sensing applications. This requires a low mechanical dissipation to dilute the signal. The mechanical dissipation is also of even more relevance for quantum measurement as it determines the lifetime of the quantum states [12].

The external perturbation acting on the resonator changes its frequency and its displacement, which can be detected by electrical or optical means [13]. One way to detect the resonator's motion with optical detection is by using coherent light, which is reflected at the resonator's surface. The reflectivity can be enhanced, and the read-out can thus be more efficient by alternating the in-plane dielectric constant of the resonator with structures called photonic crystals [14]. The coupling between the electromagnetic radiation and the resonator can be enhanced even further, and quantum mechanical motion detection can be achieved by cavity optomechanical techniques. Here, the cavity enhances the intensity of the electromagnetic radiation by confining it to a compact space [15].

The downscaling also comes with some drawbacks. Small dimensions of micromechanical resonators entail an increased surface-to-volume ratio. This enhanced ratio results in mechanical losses at the resonator's surface and enhanced dissipation [16], [17]. However, the dissipation can be significantly reduced by choosing a suitable material, design, and operating environment for the resonator. The most commonly and former leading material for micromechanical resonators is highly stressed amorphous silicon nitride (Si_3N_4), where the stress acts as additional storage of energy and thus dilute the dissipation [18]. Si_3N_4 is often used as it can be deposited on silicon and is thus compatible with commonly known nanofabrication equipment and procedures. However, Si_3N_4 has received competition from crystalline materials

such as silicon carbide (SiC) , silicon (Si) and indium gallium phosphide (InGaP) during the last years due to their potentially low intrinsic dissipation and high yield strength. Yield strength is a measure of the amount of tensile stress which a material can be exposed to before it deforms beyond repair [19]. State-of-the-art micromechanical resonators have shown plenty of different one- and two-dimensional designs to minimize dissipation. A selection of these is shown in Figure 1.1.

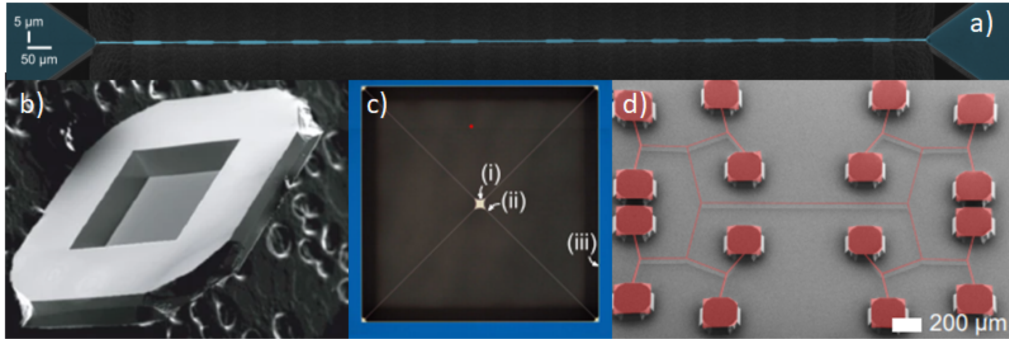

Figure 1.1: SEM images of different geometries used in state-of-the-art micromechanical resonators. a) is a string with alternating width taken from Ref. [18], b) is a membrane taken from Ref. [20], c) is a trampoline taken from Ref. [21] and d) consists of multiple branches of strings taken from Ref. [22].

1.1 Thesis organization

This thesis aims to design micromechanical resonators made of tensile stressed crystalline InGaP with low mechanical dissipation. Simultaneously, a low optical loss is necessary for these resonators as their motions are detected via optical means. The mechanical dissipation is minimized by introducing tensile strain to the material and altering the resonators' geometry. Furthermore, the resonators' motions are measured at low pressures to avoid dissipation from the surrounding medium. On the other hand, the optical loss is reduced by implementing photonic crystals. The aim of this thesis is accomplished through three steps:

- Firstly, the material's intrinsic properties, such as inherited stress and dissipation that originates from the material, are determined. This is done by comparing the experimentally observed resonance frequencies and quality factors of fabricated strings to analytical models. The design of these strings can be seen in Figure 1.2a.
- Secondly, the mechanical dissipation is minimized by altering the dimensions of a trampoline-shaped micromechanical resonator, shown in Figure 1.2b. This is done with finite element method simulations. The optimized design is then fabricated and characterized at different pressures and temperatures.
- Lastly, the coupling between the resonator and light is enhanced by tuning the design of photonic crystals via simulations. The design is then fabricated, and its reflectivity is measured.

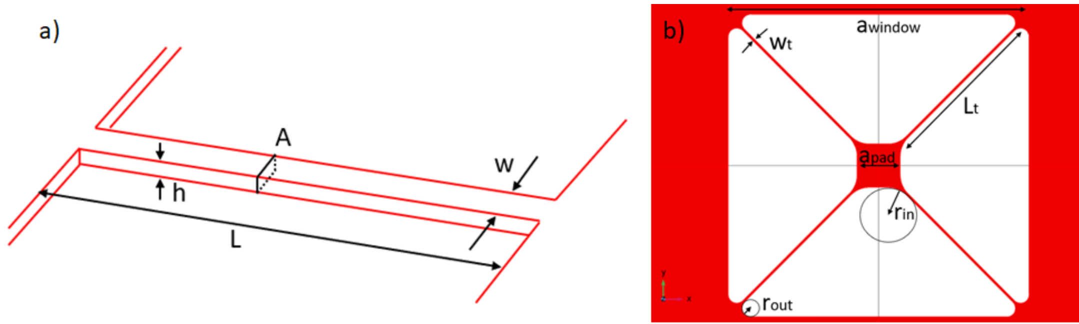

Figure 1.2: Schematics illustration of the two kinds of resonators which are treated in this thesis. a) shows a doubly-clamped string with height h, width w, length L and cross-section area A shown. A trampoline-shaped resonator is shown in b), consisting of a pad with with a_{pad} and four tethers with width w_{t} and length L_{t}. The window size of the trampoline is a_{window}. The widening of the clamping points between the tethers and the supporting structure are determined by r_{out}, while the radius r_{in} determines the transition between the tethers and the pad.

2
Theory

This chapter introduces the theoretical background necessary to understand this thesis. Firstly, the behavior and characteristics of a mechanical resonator are presented, followed by a discussion of how these can be improved. Lastly, the concept of photonic crystals is presented.

2.1 Basic concept behind a mechanical resonator

The first part of this chapter describes the standard description of a classical harmonic oscillator. However, micromechanical resonators that operate in the quantum regime and detect small distances and forces are affected by quantum limitations. Hence, these limitations are also essential to take into consideration.

2.1.1 Classical description

A simple harmonic oscillator, illustrated in Figure 2.1, can be described by a system with an effective mass m and spring with an effective spring constant k. The position of the center of the mass is represented by $x(t)$. The mass oscillates around its equilibrium with a resonance frequency (ω_m):

$$\omega_\mathrm{m} = \sqrt{\frac{k}{m}} \tag{2.1}$$

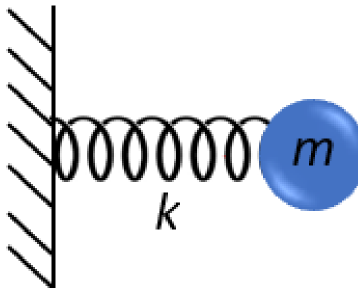

Figure 2.1: Schematic illustration of a simple harmonic oscillator with effective mass m and effective spring constant k.

The equation of motion for a damped harmonic oscillator, driven by a force F_{ext} is:

$$m\left(\frac{d^2x(t)}{dt^2}+\Gamma\frac{dx(t)}{dt}+\omega_{\text{m}}^2x(t)\right)=F_{\text{ext}} \tag{2.2}$$

where the rate at which energy dissipates from the resonator is known as the mechanical damping rate (Γ). The dissipation is often set in relation with the resonance frequency of the resonator to see the amount of dissipation per oscillation. This is known as the *Quality factor* (Q) and is given by:

$$Q=\frac{\omega_{\text{m}}}{\Gamma} \tag{2.3}$$

The simplest solution for Equation 2.2 is when the resonator is not driven, i.e. $F_{\text{ext}}(t)=0$, and is expressed as [12], [23]:

$$x(t)=A_0e^{\frac{\Gamma t}{2}}\sin\left[\sqrt{\omega_{\text{m}}^2-\left(\frac{\Gamma^2}{4}t\right)}+\phi\right] \tag{2.4}$$

where ϕ is the phase and A_0 is the initial amplitude of the oscillation, i.e. $A_0=x|_{\text{t=0}}$. For an underdamped resonator ($\Gamma<2\omega_{\text{m}}$), Equation 2.4 can be approximated as:

$$x(t)=A_0\cos(\omega t+\phi)e^{-\frac{\Gamma t}{2}} \tag{2.5}$$

and is illustrated in Figure 2.2.

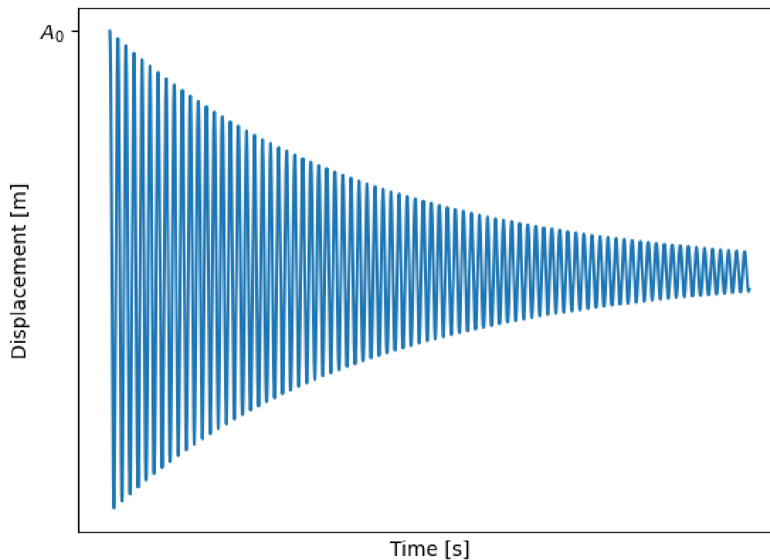

Figure 2.2: Illustration of the motion of an damped harmonic oscillator as a function of time, see Equation 2.5.

The equation of motion for a driven oscillator can be described by the Fourier transform [1] of Equation 2.2 as follows:

$$\hat{F} = m(\omega_\mathrm{m}^2 - \omega^2 - i\Gamma\omega)\hat{x}(\omega) \tag{2.6}$$

and can be rewritten as:

$$\hat{x}(\omega) = \chi\hat{F} \tag{2.7}$$

χ is the susceptibility and given by:

$$\chi(\omega) = \frac{1}{m(\omega_\mathrm{m}^2 - \omega^2 - i\omega\Gamma)} \tag{2.8}$$

Thus, the amplitude of the resonator increases as $\omega \rightarrow \omega_\mathrm{m}$ [15], [24].

The smallest signal a resonator can detect is determined on its sensitivity. According to the fluctuation-dissipation theorem, the sensitivity to detect a physical quantity A is given by $\sqrt{S_\mathrm{AA}(\omega)}$. Here, $S_\mathrm{AA}(\omega)$ is the noise power spectrum and is given for the displacement x as [12], [23]:

$$S_\mathrm{xx}(\omega) = \int_{-\infty}^{\infty} \langle x(\tau)x(0)\rangle e^{i\omega t} \tag{2.9}$$

The fundamental limit to detect a force is set by the thermo-mechanical noise which is:

$$F_\mathrm{th} = \sqrt{S_\mathrm{FF}} = \sqrt{4k_\mathrm{B}Tm\Gamma} \tag{2.10}$$

where k_B is Boltzmann's constant. Inserting Equation 2.10 into 2.7 gives us the sensitivity of displacement due to thermal noise near the resonance frequency:

$$\sqrt{S_\mathrm{xx}(\omega)} = \sqrt{|\chi|^2 F_\mathrm{th}^2} = \sqrt{\frac{2\Gamma k_B T}{m((\omega_\mathrm{m}^2 - \omega^2)^2 - \omega^2\Gamma^2)}} \tag{2.11}$$

where T is the temperature of the thermal bath and k_B is Boltzmann's constant. Thus, both the force and displacement sensitivity depend on the dissipation of the mechanical resonator [12]. It is therefore important to have a small dissipation and thus a large quality factor to obtain highly sensitive resonators.

2.1.2 Quantum description

Harmonic oscillators can also be described from a quantum point of view. The Hamiltonian for a harmonic oscillator is given by:

$$H = \hbar\omega_\mathrm{m}\hat{b}^\dagger\hat{b} + \frac{1}{2}\hbar\omega_\mathrm{m} \tag{2.12}$$

where $\hat{b}^\dagger$ and $\hat{b}$ is phonon creation and annihilation operator respectively, described by:

$$\hat{b}^\dagger = \frac{1}{2x_\mathrm{ZPF}}(\hat{x} + \frac{i}{m\omega_\mathrm{m}}\hat{p}) \quad \text{and} \quad \hat{b} = \frac{1}{2x_\mathrm{ZPF}}(\hat{x} - \frac{i}{m\omega_\mathrm{m}}\hat{p}) \tag{2.13}$$

[1] Fourier transform defined as $\hat{F}(\omega) = \int_{-\infty}^{\infty} x(t)e^{-i\omega t}dt$

where x_{zpf} is the zero point fluctuation and is given by:

$$x_{\mathrm{zpf}} = \sqrt{\frac{\hbar}{2m\omega_{\mathrm{m}}}} \tag{2.14}$$

The zero point fluctuation quantifies the lowest possible amplitude of the quantum mechanical resonator. $\hat{x}$ and $\hat{p}$ are the position and momentum operator respectively, and satisfies the commutation relationship $[\hat{x}, \hat{p}] \geq i\hbar$, which is known as Heisenberg's uncertainty [25].

In order to achieve measurement-based quantum control, the loss due thermal decoherence most be less than the frequency of the oscillation:

$$\omega_{\mathrm{m}} > \bar{n}\Gamma \tag{2.15}$$

where $\bar{n}$ is the average phonon number and is given by $\bar{n} = \langle \hat{b}^{\dagger}\hat{b} \rangle$ [15]. In other words, the oscillation needs to undergo at least one coherent mechanical oscillation before one phonon from the thermal bath enters the system. This can be translated to [26]:

$$Q_{\mathrm{m}} f_{\mathrm{m}} > \frac{k_B T}{h} \tag{2.16}$$

Thus, both the classical and quantum limit for the sensitivity of a resonator is direct affected by the quality factor.

2.2 Sources of Mechanical Dissipation

The most fundamental definition of Q is the ratio between the total energy stored in a micromechanical resonator (W) and the amount of energy that is dissipated during one of its oscillations (ΔW)[13], [27],

$$Q = 2\pi \frac{W}{\Delta W} \tag{2.17}$$

In order words, Q describes how well the resonator stores energy and how many coherent oscillations it undergoes before its amplitude decays to a certain threshold, namely $e^{-\pi}$ [28]. As was seen in Section 2.1.1, a large quality factor is desirable as it yields a more precise and sensitive readout [7], [29], [30]. Q can be divided into an intrinsic (Q_{int}) and an extrinsic (Q_{ext}) quality factor as follows:

$$Q^{-1} = Q_{\mathrm{int}}^{-1} + Q_{\mathrm{ext}}^{-1}$$

(2.18)

Both of these two dissipation mechanics have contributions from various processes, such as thermoelastic-, gas- and clamping loss. The largest source of dissipation sets the limit for Q [7], [13]. In the following, the most important intrinsic and extrinsic loss mechanisms pertinent to micromechanical resonators, particularly crystalline mechanical resonators, are discussed. More detailed discussions can be found in the reviews by Imboden [29] and Schmid [13].

2.2.1 Intrinsic dissipation

Intrinsic dissipation is material dependent and originates due to the most fundamental property of a resonator - oscillation. A direct consequence of oscillations for a resonator is bending and deformation of the resonator. This results in oscillating strain, stress, and friction between atoms within the resonator. During oscillation the potential energy, stored as bending and elongation energy, is converted to kinetic energy and vice versa. This alternating energy conversion generates heat and thus energy loss. Hence, the intrinsic quality factor for a resonator is given by:

$$Q_{\text{int}} = 2\pi \frac{W_{\text{Elongation}} + W_{\text{Bending}}}{\Delta W_{\text{Elongation}} + \Delta W_{\text{Bending}}} \tag{2.19}$$

where W_{Bending} and $W_{\text{Elongation}}$ is the potential energy stored as bending and elongation, respectively, while $\Delta W_{\text{Elongation}}$ and $\Delta W_{\text{Bending}}$ is the energy loss during one oscillation.

The intrinsic quality factor has two main contributions: *friction*-(Q_{Friction}) and *fundamental loss* ($Q_{\text{Fundamental}}$). The former process originates from friction between atoms that occurs during oscillation of the resonator. This results in a phase shift between the strain and stress within the material which in turn results in energy loss. Friction loss is largest for amorphous materials, in comparison with crystalline materials, due to the large friction between molecular chains [13]. On the other hand, fundamental loss originates from intrinsic properties of the material, such as the thermoelastic coefficient. *Thermoelastic damping* and damping due to *Two Level System* (TLS) are examples on fundamental losses mechanisms[13], [29]. These two processes will be explained in the following.

2.2.1.1 Thermoelastic dissipation

During oscillation of a micromechanical resonator, a few regions are compressed while other are elongated. The compressed regions are heated, while the stretched regions are cooled [31]. This thermal gradient results in an energy transfer in the form of phonons from the hot to the cold regions. The stream of phonons is an irreversible process and thus generates energy loss [28]. This source of energy loss is known as *Thermoelastic disipation* (TED). Q_{TED} is described as the following for a double clamped beam [2]:

$$Q_{\text{TED}}^{-1} = \frac{\alpha^2 T E}{\rho C_p} \frac{\omega \tau_{\text{TED}}}{1 + (\omega \tau_{\text{TED}})^2} \tag{2.20}$$

where T is the temperature at the resonator's surface, ρ is the mass density, C_p is the specific heat constant at constant pressure and E is Young's modulus. τ_{TED} is the thermal relaxation time and is given by:

$$\tau_{\text{TED}} = \frac{h^2 \rho C_p}{\pi^2 \kappa} \tag{2.21}$$

[2] A few approximations are made to obtain Equation 2.20. Approximations such that the boundary conditions were fixed and heat flow perpendicular to the surface were assumed to be neglected.

where h is the thickness of the resonator and κ is the thermal conductivity. α is the *Linear thermal expansion coefficient*. The thermal expansion coefficient is material dependent and is a quantification of how well the acoustic phonons are coupled to the thermal phonons and is given by [29], [31]:

$$\alpha = \frac{1}{L}\frac{\delta L}{\delta T} \tag{2.22}$$

Here, $\frac{\delta L}{\delta T}$ is the change of length due to a temperature change and L is a characteristic length. α for indium phosphide (InP), gallium phosphide (GaP) and InGaP in relation to the temperature is illustrated in Figure 2.3 [32].

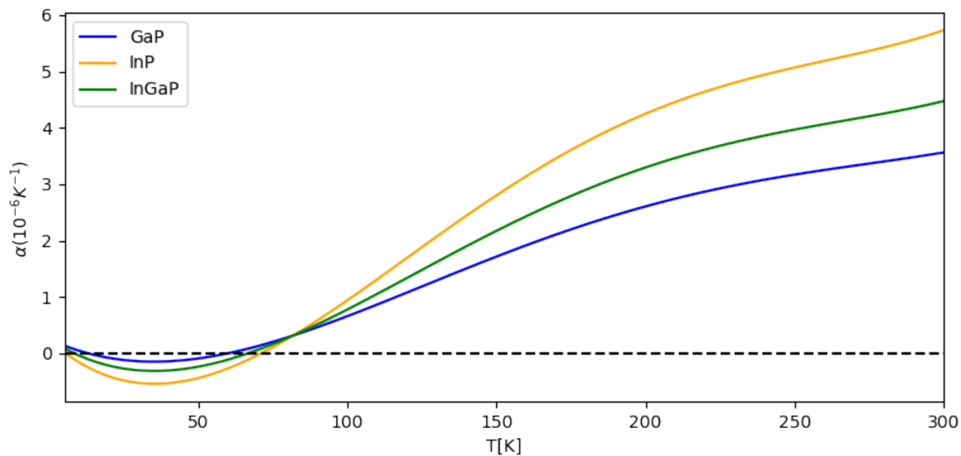

Figure 2.3: The thermal expansion coefficient α as a function of temperature for three different materials - GaP, InP and InGaP. Data points for GaP and InP are taken from [32]. An interpolation between the two curves is then made to obtain the curve for $In_{1-x}Ga_xP$ with a Ga content of x=0.58.

It can be seen in Figure 2.3 that α, and therefor TED, is more pronounced at room temperature and decreases as $\alpha \rightarrow 0$ [32] Hence, the temperature significantly affects Q_{TED} [29]..

2.2.1.2 Dissipation through TLS

TED losses are expected to be negligible at low temperatures. However, for these temperatures another source of intrinsic dissipation is more pronounced, namely dissipation due to two-level systems (TLS). This dissipation mechanism is due to quantum-mechanical phonon tunneling between metastable energy levels $|u\rangle$ and $|z\rangle$, shown in Figure 2.4. Between the two metastable levels is a potential barrier V, which is larger than the thermal energy ($V \gg k_B T$). Therefore, an energy transition between these nearly degenerated ground states is impossible at a classical level. However, a phonon can tunnel between the two states. This tunneling results either in a phonon q being absorbed or emitted. Amorphous materials have a lot of metastable energy levels due to the large amount of defects within them. Hence,

more significant dissipation due to TLS is found in amorphous materials compared to crystalline materials [29], [33].

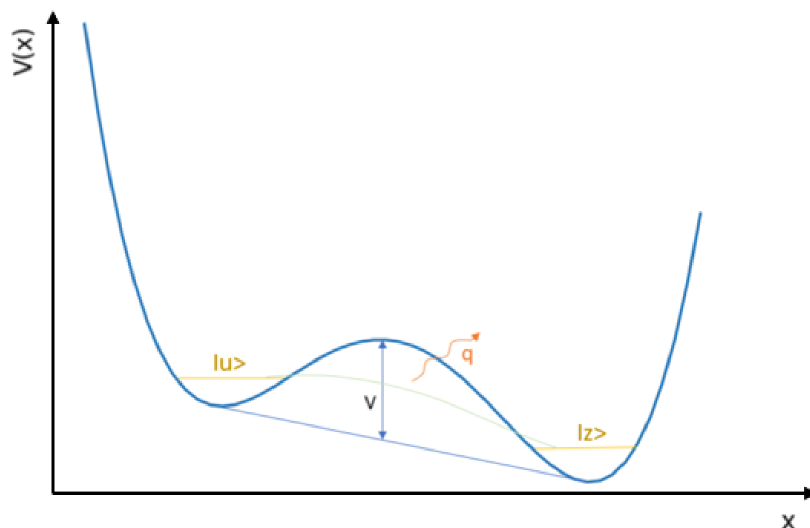

Figure 2.4: Schematic illustration of tunneling between two energy levels $|u\rangle$ and $|v\rangle$. The phonon tunnels from a larger energy level to a lower, and emitting a phonon q in the process. This figure is highly inspired by images from sources [29] and [33].

2.2.1.3 Surface losses

Surface loss is a pronounced source of dissipation for micromechanical resonators as their surface-to-volume ratio is large. The dissipation is a result of surface roughness and impurities. These often emerge during the deposition of the material but can also occur later as the material reacts with the environment. For instance, dangling bonds in SiN and Si bind to oxygen when in contact with air and form an oxide layer on the surface. These surface defects can be the limiting loss process for the intrinsic quality factor of the material. However, for single crystalline materials, such as silicon carbide (SiC) or diamond, the surface loss is less pronounced as they are not as prone as amorphous materials to react with their surrounding [13], [28]. The quality factor due to surface loss for a single clamped beam is given by [29]:

$$Q_{\mathrm{SL}}^{-1} = \frac{2\delta(3w+h)}{wh}\frac{\mathfrak{Im}(E^S)}{\mathfrak{Re}(E)} \tag{2.23}$$

where δ and E^S are the thickness and Young's modulus for the surface layer, respectively. On the other hand, E is the complex modulus of the bulk and h is the thickness of the resonator [29].

2.2.2 Extrinsic

Extrinsic dissipation depends on the geometry of the resonator and its surrounding. A selection of the most pronounced extrinsic loss mechanics is discussed here [7].

2.2.2.1 Clamping losses

Dynamic strain and elastic energy are generated near and at the clamping points when a mechanical resonator oscillates. This strain will subsequently induce acoustic waves, carrying energy from the resonator to the supporting structure. This dissipation is known as clamping or radiation loss. Clamping loss depends on the acoustic impedance mismatch between the substrate and the resonator. A enhanced mismatch makes it harder for the acoustic wave to propagate into the substrate. Furthermore, clamping loss is heavily influenced by the geometry of the resonator, and more specifically, the geometry at the clamping points [7], [13], [28], [29]. A simple analytical model to describe the clamping loss for a singly clamped string was derived in [29] and results in:

$$Q_{\mathrm{clamp}}^{-1} \approx 0.31\frac{w}{L}(\frac{h}{L})^4 \tag{2.24}$$

where w, L, and h are the string's width, length, and thickness, respectively. However, a general analytic equation for Q_{clamp} of stressed strings or more complicated geometries such as trampolines is not straightforward [7]. It is therefore convenient to use simulation based on Finite Element Methods (FEM) to determine the clamping losses for more complex structures, which is discussed in detail in Section 3.1.1 [13].

2.2.2.2 Gas damping

Gas damping originates from the medium that surrounds the resonator. Microresonators have a large surface-to-volume ratio which makes the damping from the surrounding more noticeable. Thus, gas damping is the dominant loss factor for micro-resonators at atmospheric pressure. There are two different types of gas damping: viscous and ballistic. The viscous regime describes the medium if the gas can be treated as a fluid. On the other hand, the ballistic regime is valid for systems where the medium consists of a small amount of particles and can thus be described by individual molecules. The dissipation regime that the system is in can be determined by the Knudsen number (K_n), which is the ratio between the length of the mean free path for the gas λ_{f} and the characteristic length of the resonator L_{r} [13], [30], [34]:

$$K_{\mathrm{n}} = \frac{\lambda_{\mathrm{f}}}{L_{\mathrm{r}}} \tag{2.25}$$

The mean free path is the average length that gas particles can travel before they collide with each other. All measurements presented in this thesis are in high vacuum ($10^{-3} - 10^{-7}$ mbar), where the mean free path is in centimeters to kilometers. Therefore, all the measurements are always performed in the ballistic regime.

Gas damping within the ballistic regime for a plate resonator is given by [13], [35]–[37]:

$$Q_{\mathrm{gas}}^{-1} = \sqrt{\frac{2}{\pi}}\frac{4}{\rho h \omega_{\mathrm{m}}}\sqrt{\frac{M_{\mathrm{m}}}{RT}}P \tag{2.26}$$

where R is the universal molar gas constant, P is the air pressure, and M_{m} is the molar mass for the medium which for air is 29 g/mol [13]. Equation 2.26 is derived from the difference in pressure between the front and back side of a plate resonator when gas molecules collide with it [35], [37]. Thus, the dissipation due to gas damping depends on the resonator's size, as it affects the resonance frequency (see Equation 2.1) and the pressure it is surrounded by.

2.3 Engineer and minimize mechanical dissipation

Most of the dissipation mechanisms discussed previously can be minimized by choosing the suitable surrounding for the resonator to operate in. For instance, thermoelastic- and gas damping can be reduced by operating the resonator at low temperature and low pressures, respectively [13]. On the other hand, clamping loss can be minimized by modifying the geometry to improve the shielding between the resonator and substrate and thus encapsulate the acoustic waves within the resonator [7].

The intrinsic dissipation for an unstressed resonator always exists for the material independently of its design and surrounding. Q_{int} can be enhanced by choosing a material with a small number of defects or by using the concept *Dissipation Dilution* [7], [27], [28]. State-of-the-art resonators have employed this concept and reached Q up to 10^{10} at low temperatures [18]. In the following, these methods to enhance the intrinsic quality factor are described together with methods to minimize clamping loss.

2.3.1 Minimizing clamping loss

The first way to minimize clamping loss, namely by increasing impedance mismatch between the resonator and the substrate, was mentioned in Section 2.3.1. The impedance mismatch can be a result of the large size and mass difference between the resonator and its substrate [7]. Another way to increase the impedance mismatch is by implementing periodic arrays with holes around the resonator known as *Phononic Crystal* (PnC), which creates an acoustic bandgap. The acoustic waves with eigenfrequencies f within this bandgap are not prone to propagate away from the resonator. The design of the PnC is important for it to work as intended. The length of a unit cell for PnC (a_{PnC}) should be [38]:

$$a_{\mathrm{PnC}} = \frac{\lambda}{2} = \frac{v}{2f} \tag{2.27}$$

where λ is the wavelength of the acoustic wave centered in the middle of the bandgap and v is the acoustic velocity in the material [38]. Thus, devices with eigenfrequencies in MHz would approximately have a_{PnC} in millimeters. Furthermore, the suppression of acoustic waves is exponentially dependent of the number of unit cells within the crystal [7]. Hence, the total size of the resonator and its PnC should at least be in centimeters to shield acoustic waves in the MHz range [38]. In other words, PnC often requires a lot of space [7]. An example of a resonator with PnC is illustrated in Figure 2.5. Here, the micromechanical resonator is in the center of

the PnC, and each square corresponds to a unit cell [39].

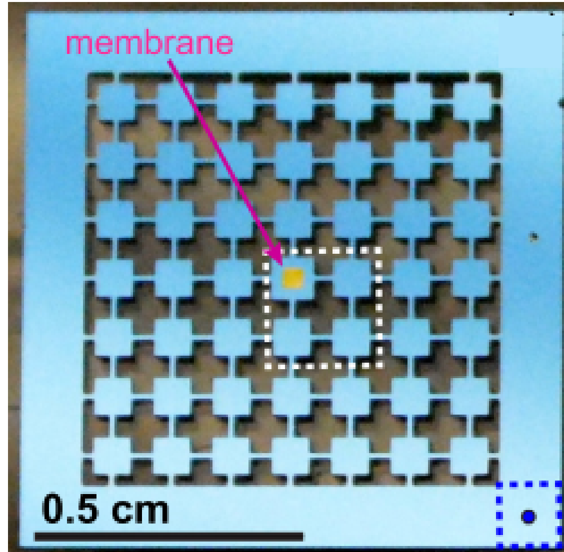

Figure 2.5: A PnC used to minimize clamping loss with a resonator (membrane) placed in the center of the PnC. Picture is taken from Ref. [38].

2.3.2 Strained resonators

The intrinsic quality factor can be increased by realizing the mechanical resonator in a material with inherent tensile stress. This method to enhance Q is known as *Dissipation Dilution*. The concept behind dissipation dilution is explained in the upcoming section, but the principle behind strain and stress is first discussed.

Intrinsic strain in the material originates from the growth process due to the difference in crystal lattice constant or thermal expansion coefficient between the alternating layers [29]. The maximum amount of stress in the material is determined by the yield strength, which is the largest amount of stress that can be deposited before the material is deformed. The in-plain strain ($\epsilon^{||}$) that occurs due to the lattice mismatch between two layers with lattice constants a_S and a_L, which are shown in Figure 2.6 [27], is given by [40]:

$$\epsilon^{||}(x) = \frac{a_\mathrm{L}^{||} - a_\mathrm{L}}{a_\mathrm{L}}, \quad a_\mathrm{L}^{||} = a_\mathrm{S} \tag{2.28}$$

Here, $a_\mathrm{L}^{||}$ is the lattice constant of the second layer when it is epitaxial grown on the substrate with lattice constant a_s. Thus, a_s and $a_L^{||}$ is approximately the same. The relation between the strain and the stress as given by Hooke's law is:

$$\sigma(x,\theta) = E(x,\theta)\epsilon^{||}(x) \tag{2.29}$$

where E is Young's modulus and is direction dependant for anisotropic materials [27].

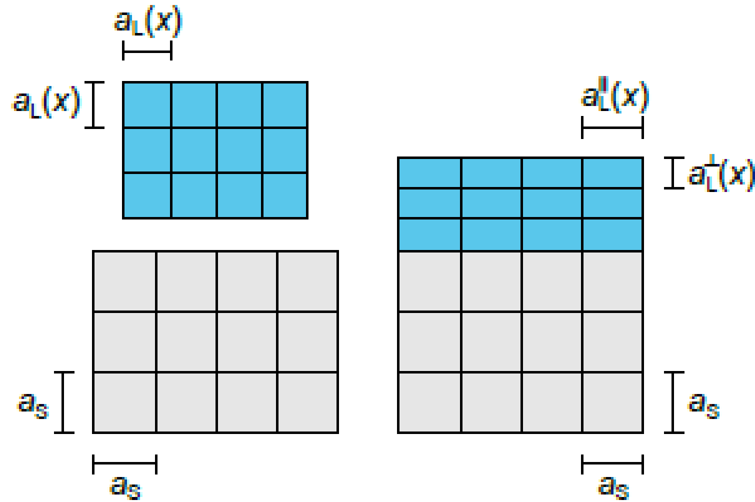

Figure 2.6: A schematic picture of the origin of strain from lattice mismatch. Gray is the substrate and blue the device layer. Picture is taken from Ref. [27].

The equation of motion for an unstressed micromechanical string resonator with a displacement field u, moment of inertia I, mass density ρ and cross-sectional area A is given by:

$$EI\frac{\partial^4}{\partial x^4}u(x,t) + \rho A\frac{\partial^2}{\partial t^2}u(x,t) = 0 \tag{2.30}$$

while the equation of motion for a resonator with an inherited stress of σ can via the generalized Euler-Bernouilli equation be expressed by [23], [28]:

$$EI\frac{\partial^4}{\partial x^4}u(x,t) - \sigma A\frac{\partial^2}{\partial x^2}u(x,t) + \rho A\frac{\partial^2}{\partial t^2}u(x,t) = 0 \tag{2.31}$$

The first term in Equation 2.30 and the two first in Equation 2.31 contribute to the potential stored energies, while the time derivatives contribute to the kinetic energies. It can be seen by comparing the two equations that unstressed resonators have an additional way to store potential energy, which depends on the stress. By solving Equation 2.31 for a sinusoidal wave with mode number n and with fixed boundary conditions:

$$U_n(0) = U_n(L) = 0$$
$$\frac{\partial^2}{\partial x^2}U_n(0) = \frac{\partial^2}{\partial x^2}U_n(L) = 0$$

the eigenfrequency of the 'n'th harmonic can be obtained and expressed as:

$$f_{\text{n}} = \frac{n^2\pi}{2L^2}\sqrt{\frac{EI}{\rho A}}\sqrt{1 + \frac{\sigma AL^2}{n^2\pi^2 EI}} \tag{2.32}$$

For high stress, $\frac{\sigma AL^2}{n^2\pi^2 EI} \gg 1$, Equation 2.32 can be approximated as[19], [40]:

$$f_{\text{n}} \approx \frac{n}{2L}\sqrt{\frac{\sigma}{\rho}} \tag{2.33}$$

There is no generalized analytical expression for f_n for stressed trampolines. However, the fundamental resonance frequency for a trampoline can be approximated by Equation 2.33 for a string resonator of length [41]:

$$L = \sqrt{2}L_{\mathrm{t}} \tag{2.34}$$

2.3.2.1 Dissipation Dilution

It have now been shown that strain in a resonator affects its equation of motion and thus the frequency and the energy stored in it. This extra storage of energy enhance the quality factor by a factor D [7], [18], [27]:

$$Q_{\mathrm{D}} = Q_{\mathrm{int}}D \tag{2.35}$$

where D is called the dissipation dilution factor and is given by [7]:

$$D = (1 + \frac{W_{\mathrm{Tensile}}}{W_{\mathrm{Elongation}} + W_{\mathrm{Bending}}}) \tag{2.36}$$

which for a string with length L, height h, mode number n and tensile stress σ can be reformulated as [27]:

$$D = (2\lambda + n^2\pi\lambda^2)^{-1} \tag{2.37}$$

where

$$\lambda = \frac{h}{L}\sqrt{\frac{\mathfrak{Re}(E)}{12\sigma}} \tag{2.38}$$

The potential tensile- (W_{Tensile}), elongation- ($W_{\mathrm{Elongation}}$) and bending energies (W_{Bending}) are all dependent on the displacement field ($u(x)$ in 1D), which is related to the mode shape $\Phi_{\mathrm{n}}(x)$ [7]:

$$u(x) = u_{0\mathrm{n}}\Phi_{\mathrm{n}}(x) \tag{2.39}$$

u_0 is the maximum amplitude for the displacement of the 'n'th mode. The mode shape for a string is given by [7], [13]:

$$\Phi_{\mathrm{n}} = \sin(\beta_\sigma x) - \frac{\beta_\sigma}{\beta_E}\Big(\cos(\beta\sigma x) - e^{-\beta_E x}\Big) \tag{2.40}$$

where

$$\beta_\sigma = \frac{n\pi}{L} \quad \text{and} \quad \beta_{\mathrm{E}} = \sqrt{\frac{\sigma A}{EI}} \tag{2.41}$$

The fundamental mode shape (n=1) for a string can be seen in Figure 2.7a. The relationships between $u(x)$ and the potential energies stored as tension, bending and elongation for a doubly clamped string can be seen in Equation 2.42, 2.43 and 2.44, respectively [7].

$$W_{\mathrm{Tensile}} = \frac{1}{2}\sigma A\int_0^{L_x}\Big(\frac{\partial u}{\partial x}\Big)^2 dx \tag{2.42}$$

$$W_{\mathrm{Bending}} = \frac{1}{2}EI_{\mathrm{y}}\int_0^{L_x}\Big(\frac{\partial^2 u}{\partial^2 x}\Big)^2 dx \tag{2.43}$$

$$W_{\mathrm{Elongation}} = \frac{1}{8}EA\int_0^{L_x}\Big(\frac{\partial u}{\partial x}\Big)^4 dx \tag{2.44}$$

It can be seen in Equation 2.42 that W_{Tensile} is proportional to σ, which is the predominant factor when the tensile stress is enhanced. Hence, W_{Tensile} increases significantly more than both $W_{\text{Elongation}}$ and W_{Bending} as the stress is increased. According to Equation 2.36, this increases the dilution factor. Furthermore, elongation and the tensile energy depend on the first derivative of the displacement — the curvature seen in Figure 2.7b. At the same time, the second derivative determines the potential energy stored in bending. The bending is shown in Figure 2.7c. Thus, it is desirable to have a small $u''(x)$ as bending decreases D. It can be seen from Figure 2.7c that $u''(x)$ is most pronounced near the clamping points of the string due to the boundary constraints, $u(0) = u(L) = 0$. However, this can be decreased by applying a method known as *Soft Clamping* which gradually decrease the amplitude of the mode shape near the attachment points. Soft clamping is described in more detail in Section 2.3.3.

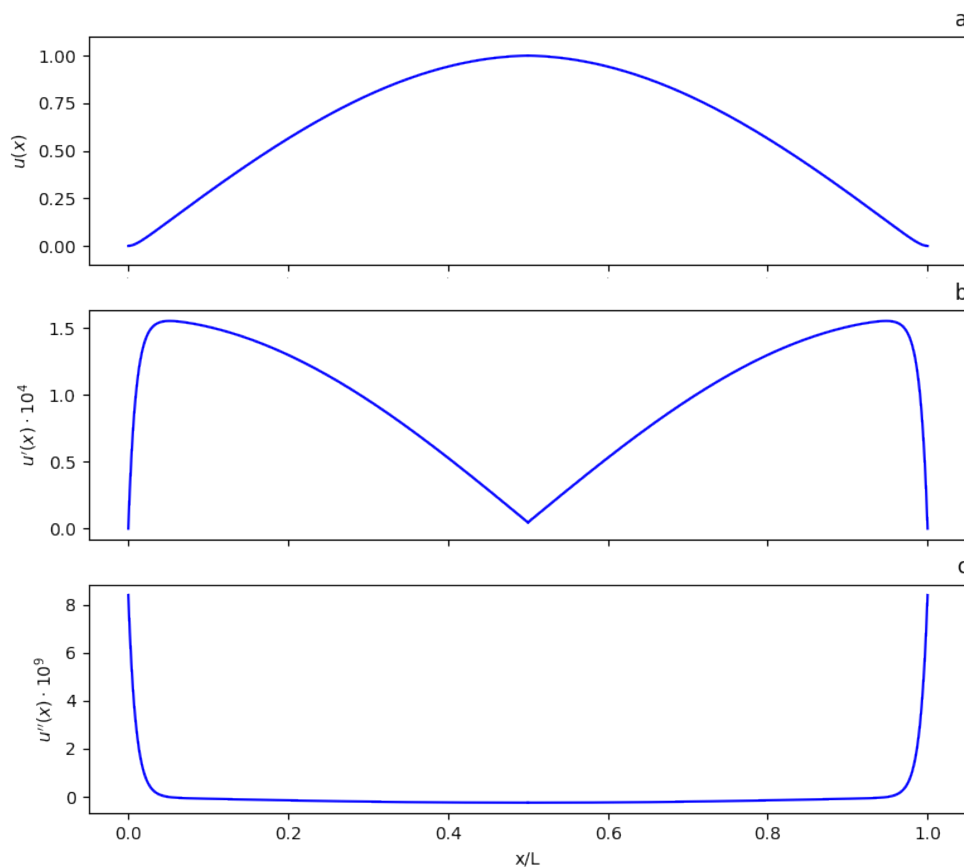

Figure 2.7: The mode shape of a tensile strained string resonator of length L and its first and second derivative in a), b) and c), respectively. b) can be seen as the curvature of the mode while c) shows the magnitude of bending. See also Refs. [7] and [13].

Lastly, for modes with a displacement field smaller than the thickness of the resonator, $W_{\text{Elongation}}$ can be neglected as $W_{\text{Bending}} \gg W_{\text{Elongation}}$. This is possible to show by using Equation 2.39, 2.42, 2.43 and 2.44 to obtain [3]:

$$\frac{W_{\text{Bending}}}{W_{\text{Elongation}}} \approx \frac{4h^2}{9u_0^2} \tag{2.45}$$

Thus, $W_{\text{Bending}} > W_{\text{Elongation}}$ as long as $2h/3 > u_0$.

2.3.3 Soft Clamping

The dissipation dilution factor can be enhanced by reducing the bending energy. In other words, minimizing $u''(x)$ near the attachment points. This can be done by engineering the geometry of the resonator in such a way that the gradient of the mode shape between the clamping point and the rest of the resonator undergoes a gradual transition, shown in Figure 2.8a. The change in bending due to this gradual transition is shown in Figure 2.8b. This method of enhancing the dissipation dilution is known as soft clamping [7].

Soft clamping has been implemented in many ways for different shaped micromechanical resonators. For instance, highly stressed trampolines have shown to utilize soft clamping as the radius of the curvature at the clamping points R are widened. This is shown in Figure 2.9a, where the mode shape for four different trampolines with $R = 0, 5, 10$ and 20 μm are shown. In the same figure, it can be seen that the gradient of the mode shape near the clamping point decreases as R increases [28], [41].

PnC has also been shown to induce soft clamping. In comparison with the previously mentioned PnC used to minimize clamping loss, PnC used for soft clamping utilizes defect modes to localize the highest amplitude of the mode in the center of the structure, far away from the clamping points [7]. Thus, no rigid clamping is imposed, and nearly no bending occurs near the clamping points. An example of a PnC that uses soft clamping together with a cross-section of its mode shape is shown in Figure 2.9b [42].

Lastly, hierarchical tensile structures are a recent approach to induce soft clamping. Resonators made of hierarchical structures utilize repeated segments with branches of different sizes to minimize the curvature of the mode near the clamping points[7], [22]. This method to implement soft clamping has resulted in Q up to 10^9 at room temperatures for Si_3N_4 resonators. An example of a hierarchical structure together with its mode shape is shown in Figure 2.9c.

[3]Where the wave is treated approximated as a sinusoidal wave and contains not the second term in Equation 2.40. This is a reasonable approximation for this purpose as the overall amplitude is of interested and not the mode shape near the clamping points.

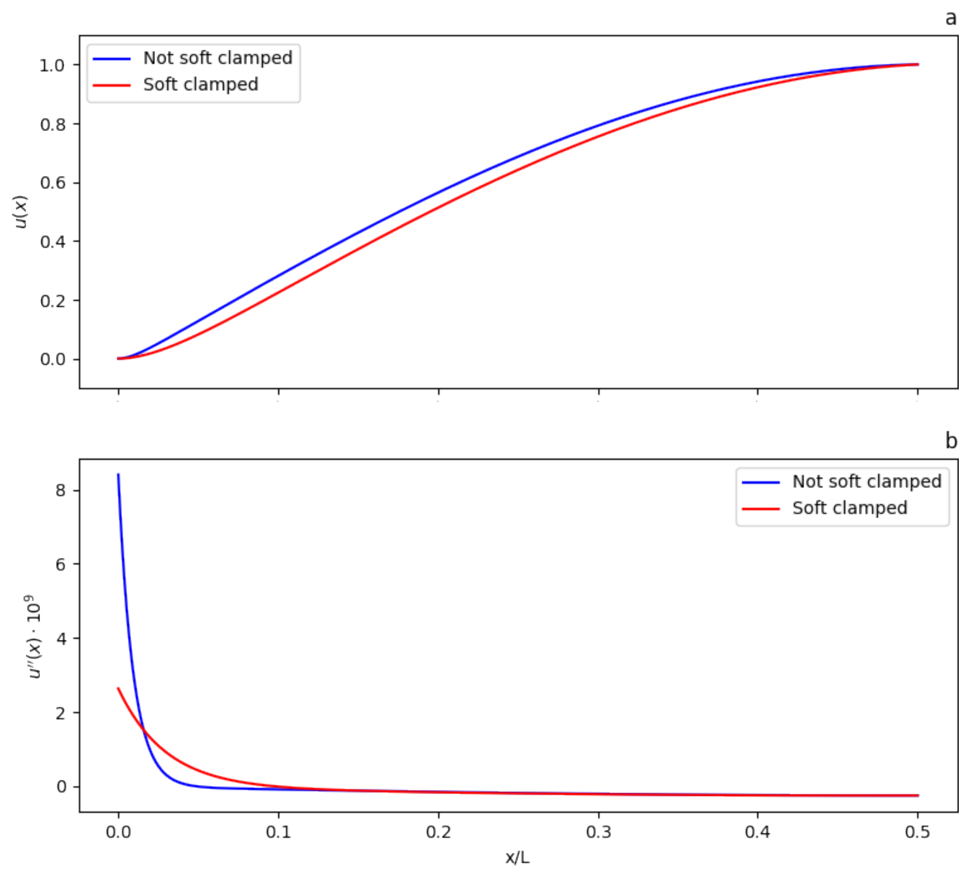

Figure 2.8: The influence soft clamping has on the mode shape and the bending ($u''(x)$) in a) and b), respectively.

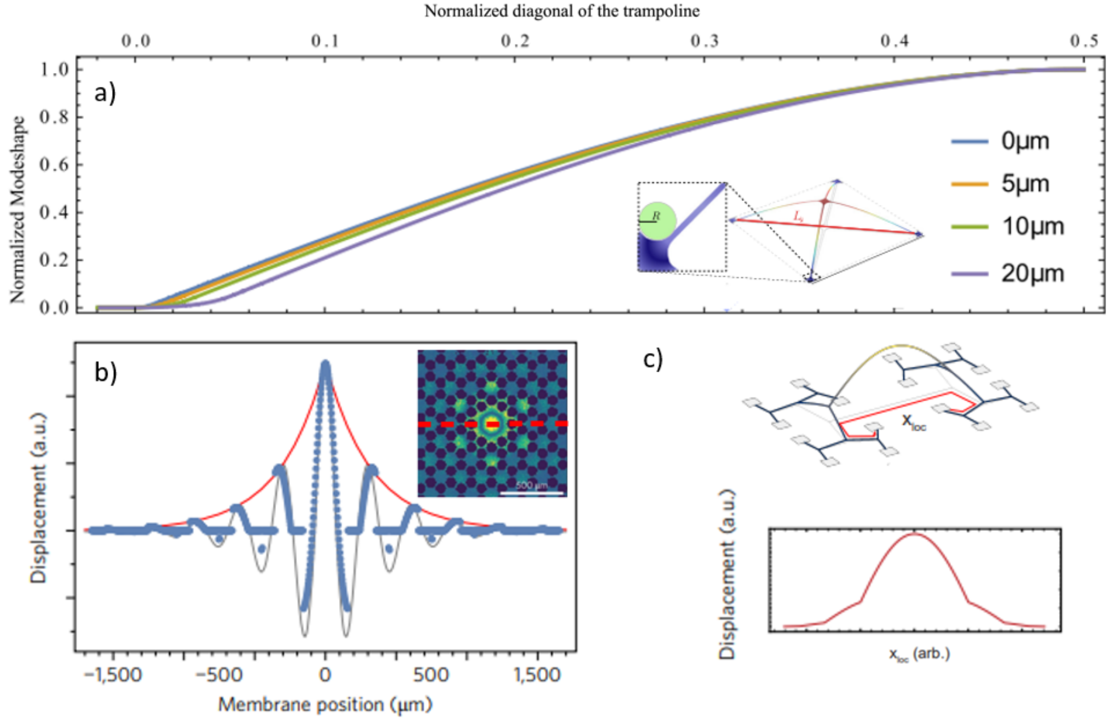

Figure 2.9: Example of different resonators that implement soft clamping. a) shows a trampoline with curvature R at the clamping points. The influence R has on the mode shape is also illustrated for $R = 0, 5, 10$ and 20 μm. This picture is taken and adapted from Ref. [5]. b) shows a PnC with a defect mode and its mode shape, taken and adapted from Ref. [42]. A hierarchical structure is illustrated in c) together with its mode shape. The red line drawn in the hierarchical structure defines the length, which is the x-axis for the mode shape. c) is taken and adapted from Ref. [22].

2.3.4 Strain engineering

Another way to enhance the dissipation dilution factor is to increase the stored tensile energy. Tensile stress is often incorporated during the growth of thin films [7]. However, stress relaxation occurs during the fabrication of the device. The magnitude of the relaxation is given by the relation [7]:

$$\sigma_{device} = (1 - \nu)\sigma_{initial} \tag{2.46}$$

where ν is the Poisson ratio, $\sigma_{initial}$ is the initial tensile stress after deposition, and σ_{device} is the stress in the resonator after suspension. Hence, the stress after relaxation is always smaller than the initial stress as $0 < \nu < 1$. However, by altering the geometry of the resonator, tensile stress can be redistributed within the resonator while keeping the total tensile force (F_T) constant. This results in some regions exhibiting larger tensile stress than the initial. The tensile force is given by:

$$F_T = A\sigma_{device} \tag{2.47}$$

where A is the area that the force is acting on. The stress redistribution depends on the geometry of the resonator, where wider regions are exposed to less stress than

the smaller regions due to the size of the cross-section area. Figure 2.10a illustrates an example of a string with localized stress. This way to enhance the stress within specific regions is known as *Strain engineering*. Strain engineering had been done chiefly for strings [18], [43], [44], but the idea has also been implemented for other structures such as trampolines [5]. For instance, it has been shown that trampolines with broader clamping points and pad sizes relative to the width of their tethers have an enhancement of tensile stress in the tethers and thus an increase in Q. Figure 2.10b shows a schematic illustration of a trampoline that uses this technique. This resonator has demonstrated Q as high as 10^8 [5].

In conclusion, dissipation dilution is a method in which tensile stress is incorporated to enhance the quality factor for micromechanical resonators. The increased strain increases the tensile energy and, thus, the dissipation dilution factor. Increased bending energy, which is most pronounced near the clamping points, decreases Q. There exist two methods to enhance the dissipation dilution by increasing the local tensile stress or minimizing the bending near the clamping points, which are known as *Strain engineering* and *Soft clamping*, respectively.

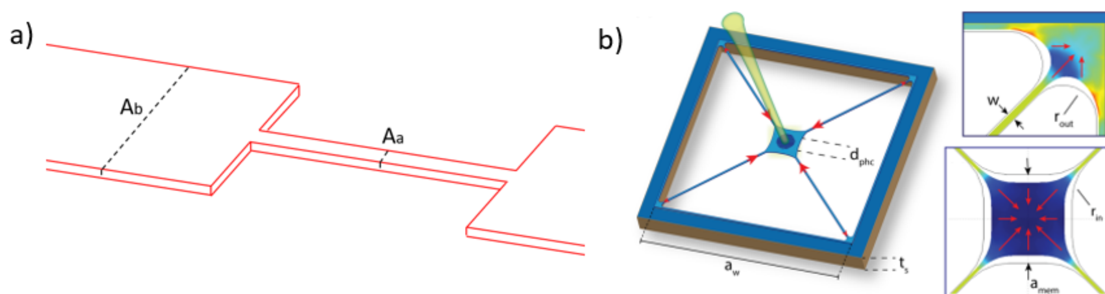

Figure 2.10: Resonators that uses strain engineering. Strain engineering for a string is shown in a). Here, strain is localized in the smaller regions denoted with 'a' and decreased in the larger regions 'b'. The cross-section area for the small and large region is denoted A_a and A_b, respectively, see Ref. [43]. b) shows a trampoline with decreased strain at the pad and at the clamping points while strain in the tethers is increased taken from Ref. [5].

2.4 Optical read-out of mechanical motion

Optical detection of mechanical motion of micromechanical resonators has shown to be a quick and simple testing method for MEMS prototypes. Interferometric technique is an optical read-out detection where two beam paths, usually from the same light source, with the same well-defined phase, are used. Here, one of the beams is a reference signal, while the other beam reflects off the measured resonator. The change in length that the light travels based on the movement of the resonator $x(t)$ induces a phase shift between this beam and the reference beam ($\Delta\Phi$) [45]:

$$\Delta\Phi = \frac{2\pi\Delta x(t)}{\lambda} \tag{2.48}$$

Here, $\Delta x(t)$ is the extra length which the reflected signal travels in comparison with the reference arm due to movement of the resonator. To obtain a clear readout, enough light must be reflected from the resonator. The reflectivity of the mechanical resonator can be tailored with the help of *Photonic crystals* (PhC)[46].

2.4.1 How the reflectivity of a mirror can be improved

Photonic crystals are periodic structures in the material, which result in periodic change of the dielectric constant [5]. These PhC structures can, for instance, be air holes illustrated in Figure 2.11a. The refractive index n gives the dielectric constant:

$$\epsilon = n^2 \tag{2.49}$$

The variation of the refractive indices at the media interfaces results in Fresnel reflection of light out of the plane, causing waves to propagate in-plane of the PhC. These waves constructively or destructively interferes with the incoming out-of-plane propagating waves resulting in transmission or reflection of the light [46]. The in- and out-of-plane propagating waves that interfere with each other are illustrated in Figure 2.11b [47]. This interference results in a photonic band gap, where all wavelengths within the bandgap are reflected from the PhC [4] [14], [39].

The design of the PhC which are used in this thesis is shown in Figure 2.11. Here, a_{PhC} and r_{PhC} are the lattice constant and the radius of the PhC respectively. The incoming beam is either s- or p-polarized and its direction can be described by the polar angle ϕ and the azimuthal angle θ. The photonic bandgap can be designed for a specific wavelength with the appropriate values of a_{PhC} and r_{PhC}. The values for a_{PhC} and r_{PhC} are obtained through optical simulations. However, some general rules for designing PhC exist in the broadband regime. For instance, a higher ratio between the radius and lattice constant ($r_{\mathrm{PhC}}/a_{\mathrm{PhC}} \sim 0.4$) have shown a greater reflection than smaller ratios ($r_{\mathrm{PhC}}/a_{\mathrm{PhC}} \sim 0.1$) [48].

[4] Note that PhC and PnC are not the same. The first mentioned treats photons while the second treats phonons

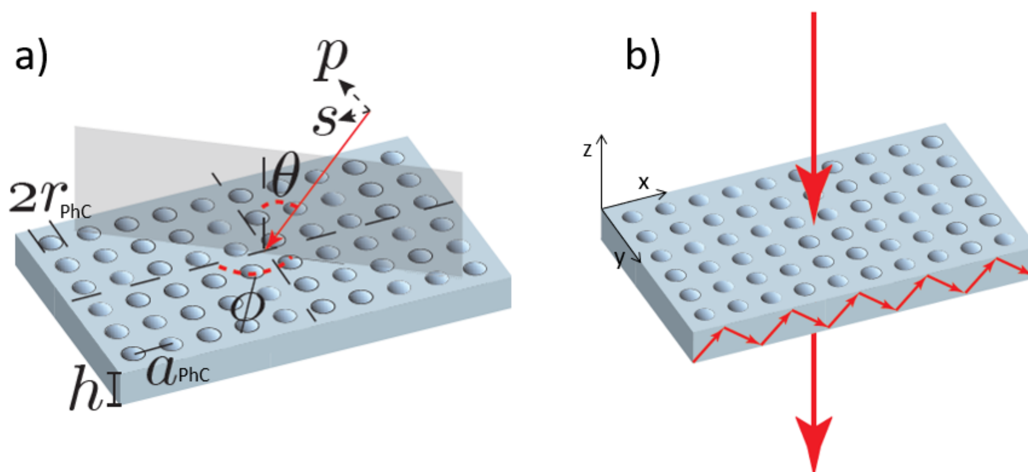

Figure 2.11: Illustration of PhC. All necessary properties of the PhC and the incoming light beam shown are shown in a). The in- and out of plane propagating waves that interfere with each other are illustrated in b) [47].

The incoming laser beam can be described by a Gaussian beam that propagates in the longitudinal direction, i.e., a direction parallel with the z-axis in Figure 2.11a. The beam size at a position z for a Gaussian beam is determined by:

$$w(z) = w_0\sqrt{1 + (\frac{z}{z_0})^2} \tag{2.50}$$

where

$$w_0 = \frac{\lambda z_0}{\pi} \tag{2.51}$$

and w_0 is the minimum value of the beam radius, also known as the waist of the beam. λ is the wavelength, and z_0 is the Rayleigh range. In other words, z_0 is the position where $w(z) = \sqrt{2}w_0$ and can be described as the divergence of the Gaussian beam. Clipping loss always occurs to an extent, as the mirror is finite, and it is given by:

$$\mathrm{L_{cl}} = e^{-\frac{1}{2}\left(\frac{D_{\mathrm{Mirror}}}{w_0}\right)^2} \tag{2.52}$$

where D_{Mirror} is the diameter of the mirror, which in this case is the size of the PhC shown in Figure 2.12. In the same figure is an illustration of the beam with a diameter $D_{\mathrm{Beam}} = 2w_0$ shown. It can be seen from Equation 2.52 that the loss decreases exponentially as the ratio between the diameter of the mirror and the beam increases[49].

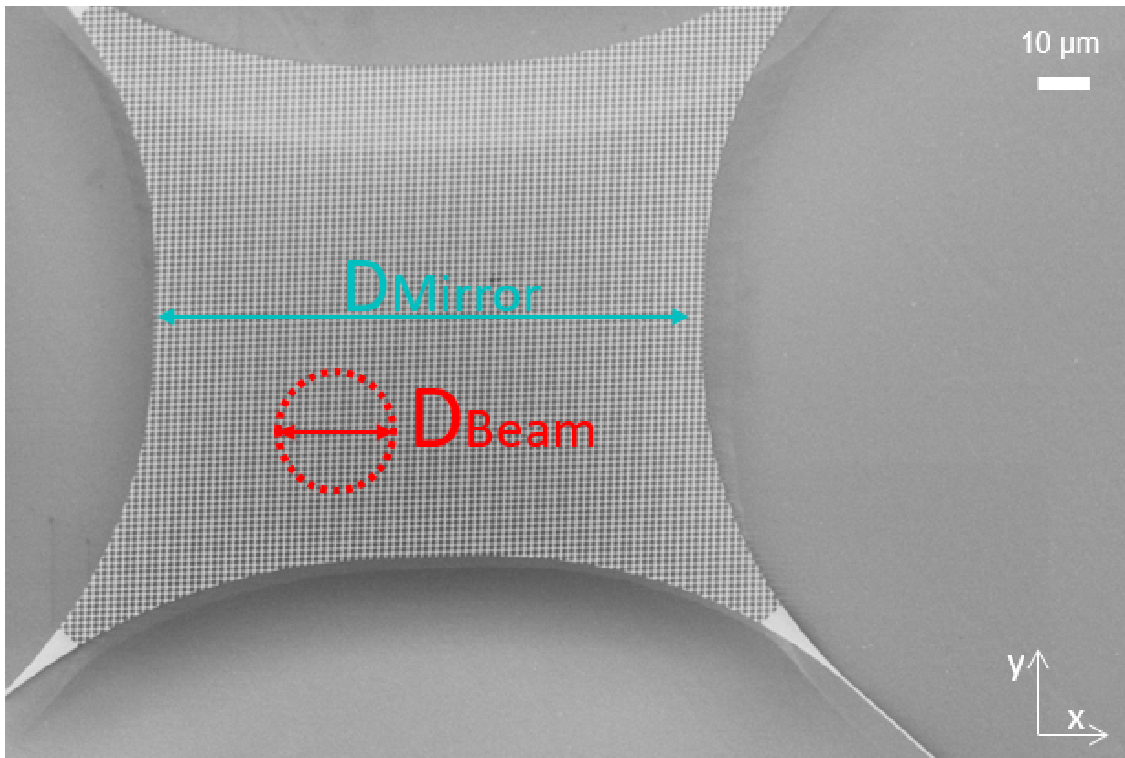

Figure 2.12: A SEM image of a PhC with a diameter of D_{Mirror} from the top together with a drawing of a beam with a diameter of D_{Beam}.

3

Methods

The micromechanical resonators are realized in multiple steps. First, the resonators' designs are decided. The designs are optimized via analytical models and simulations to obtain micromechanical resonators with low mechanical dissipation and a fundamental mode within the kHz-MHz range. Also, the resonators should have high reflectivity at the wavelengths of interest — $\lambda = 1550$nm. This will be realized using a PhC with appropriate parameters calculated via optical simulations. Resonators with the optimized geometries are then fabricated, and the mechanical and optical properties of the micromechanical resonators are characterized to obtain Q and the reflectivity, respectively.

Figure 3.1a shows an illustration of the cross-section of the wafer used to fabricate the resonators in this thesis. The substrate is made of gallium arsenide (GaAs), while the epitaxially grown layer is indium gallium phosphide ($In_{1-x}Ga_xP$) with a Gallium concentration of x = 0.58. InGaP is an anisotropic material. Thus, the crystal direction affects the material's properties, such as the etch rate and stress distribution. An illustration of the crystal directions for a {100}-plane wafer used in this thesis is shown in Figure 3.1b.

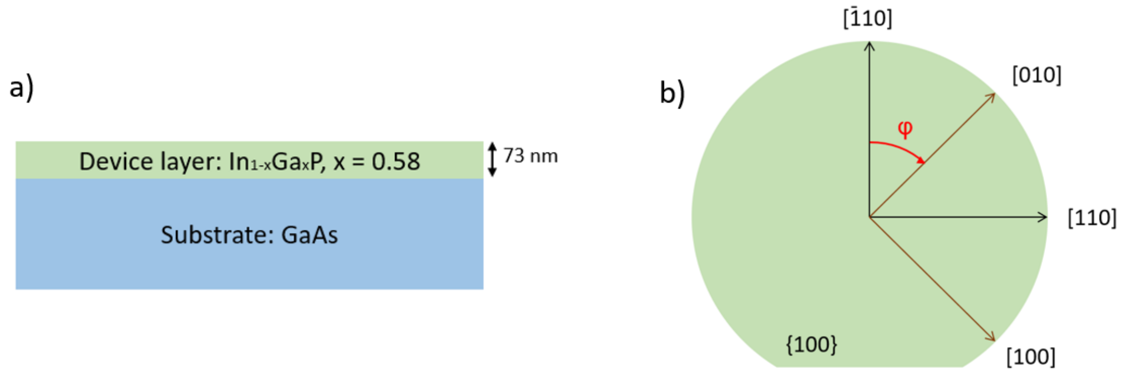

Figure 3.1: Schematic illustration of the wafer used in this thesis, in a side- and top view for a) and b), respectively. The substrate and device layer are illustrated together with the height of the device layer in a). b) illustrates all relevant lattice directions for a {100} plane wafer.

3.1 Simulations

As mentioned in Section 2.2, the mechanical resonance frequency and quality factor of micromechanical resonators depend on their design and can be described by analytical models. However, these analytical models are often approximated and only valid for simply or doubly clamped strings. Therefore, different simulation tools are often used to determine the mechanical properties of resonators with complicated geometries. Similarly, analytical calculations of the reflectivity, such as the transfer matrix, do not consider all physics of the PhC. Instead, the reflectivity for PhC is more closely obtained by optical simulations. All relevant data and properties used for the simulations are reported in Table 0.2 and Appendix A.1.

3.1.1 FEM simulations of mechanical properties

It was discussed in Section 2.3.1 that there is no general analytic function to describe clamping loss for resonators with intricate geometries. Therefore, finite element method (FEM) solvers are often used to calculate clamping loss [7], [13]. FEM is used to solve partial differential equations (PDEs) numerically. PDEs are often used to describe time and space-dependent problems and have no analytical solutions. Instead, the PDEs are solved analytically by approximated equations constructed for different discretizations [50].

COMSOL Multiphysics is a FEM simulation program that combines different physics modules to analyze complex physical problems and is used in this thesis to simulate the mechanical properties. The discretization of the geometry in COMSOL is made by meshing. There are plenty of ways to mesh models in COMSOL. The different types of mesh used for all the computations done in this thesis are illustrated in Figure 3.2. The choice of mesh depends on multiple factors, such as the dimension of the structure. Morover, the ratio between the largest and smallest features influences the mesh and whether the geometry is symmetric. Lastly, the size and type of mesh used also affects the computational time [51].

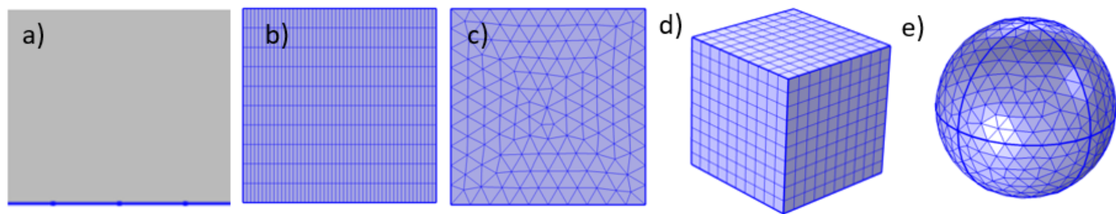

Figure 3.2: The different kinds of mesh are used in this thesis. a) shows an one-dimensional mesh called *Edge*. b) and c) are two-dimensional meshes named *Free triangular* and *Mapped* mesh, respectively. The three-dimensional meshes are called *Sweep* and *Free tetrahedral* and are shown in d) and e), respectively.

The solid mechanics Physics module is used in this thesis where a combination of Stationary and Eigenfrequency solvers are used to calculate the mechanical prop-

erties. The stationary displacement as a result of intrinsic stress is calculated by stationary solvers. Furthermore, the redistribution of the stress due to the geometry of the resonator is also a stationary calculation. On the other hand, eigenfrequency study is used to obtain the resonator's resonance frequencies. Furthermore, an eigenfrequency study determines the mode shape for the resonance frequencies. This provides an essential insight into how the mode shape is influenced by the geometric design of the resonator. Thus, the clamping loss and the magnitude of soft clamping can be estimated [52]. Lastly, the mechnical modes' quality factor can also be obtained by an eigenfrequency study if combined with a perfectly matched layer (PML). The finite PML absorbs the elastic wave that propagates away from the resonator. In other words, the energy which propagates across the clamping point would be reflected back at the end of the device if a PML was not present. Thus, no energy would dissipate, which is an ideal but inaccurate representation of reality [13]. PML is not a boundary condition but can be seen as a domain with an anisotropic and complex-valued permittivity and permeability. Hence, no elastic wave should be reflected if the PML is designed correctly. The design for a PML should consider the mesh, size, and placement of the PML. The width of the PML w_{PML} should be at least:

$$w_{\mathrm{PML}} \geq \frac{\lambda_{\mathrm{PML}}}{2} = \frac{v}{2f} \tag{3.1}$$

to absorb all elastic waves. Here, v is the velocity at which the acoustic waves propagate within the material, f is the resonance frequency at the mode of interest, and λ_{PML} is the wavelength of the acoustic wave. Furthermore, the placement of the PML is also important; if the PML is close to the radiation source, reflection at the PML's interface occurs. This can be avoided by placing the PML with a distance of $w_{\mathrm{buffer}} = \frac{\lambda_{\mathrm{PML}}}{8}$ from the radiation source [53].

3.1.2 Simulations of optical reflection

A PhC can improve the reflectively and thus the optical read-out of the resonator's motions. Reflectively of periodic dielectric structures can be simulated with Stanford Stratified Structure Solve (S^4). S^4 is based on Rigorous Coupled Wave Analysis (RCWA), and the scattering matrix formalism [54]. RCWA is a semi-analytical form of Maxwell's equation in Fourier space [55] and applies to systems with periodic changes in the dielectric constant, such as PhC. In other words, for systems that are inhomogeneous in the xy-plane but homogeneous in the z-direction, see Figure 2.11a. The main advantage for RCWA in comparison with only using the transfer matrix is the way to handle anisotropy within the material [56]. However, one limitation with the software S^4 is that it assumes that the transverse direction periodicity is infinite. Furthermore, the software only simulates plane waves, whereas a Gaussian electromagnetic wave is used for measurements. However, a Gaussian beam with a finite waist w_0 can be reconstructed by multiple plane waves from different angle of incidence. The reflection is then given by [57]:

$$R_{s,p}(\lambda, w_0) = \frac{\int\int |r_{s,p}(\phi,\theta,\lambda)|^2 e^{-\frac{1}{2}(w_0 k_{\mathrm{r}} \sin(\phi))^2} d\phi d\theta}{\int\int e^{-\frac{1}{2}(w_0 k_{\mathrm{r}} \sin(\phi))^2} d\phi d\theta} \tag{3.2}$$

Here θ and ϕ are the azimuthal and polar angle illustrated in Figure 2.11, respectively. $r_{s,p}$ is the reflectivety of a s-polarized plane wave, w_0 is the waist and k_r is the wave number.

3.2 Fabrication

This section consists of an overview of the steps involved in fabricating the micromechanical resonators. The wafers used to fabricate the resonators in this work were obtained from Professor Strittmatter's group (Magdeburg, Germany). The fabrication included pre-processing, patterning, pattern transfer, and realization of the devices. All the fabrication steps are illustrated in Figure 3.3.

Figure 3.3: An illustration of the chip after each fabrication step. The chip at the start consists of a GaAs layer (blue) and an InGaP layer (green). An adhesion promoter (yellow) and resist (red) is spin-coated to the chip in a). The exposed regions of the resist are then removed in b) by developing. This is followed by dry-etching of the GaAs layer in c). The resist and adhesion promoter is then removed by a remover and hydrofluoric acid, respectively, in d). The resonators are then suspended in e) by wet etch with citric acid and hydrogen peroxide and dried with a critical point dryer.

The first step of the fabrication process was to dice the wafer into chips, which was done mechanically with a diamond scriber along the $[\bar{1}10]$ and $[110]$ directions. The cleaning afterwards was done in acetone, isopropanol (IPA), and deionized water (DIW) to remove dirt and residues.

The diameter of the holes in the PhC, which is in the sub-micron range, is the smallest feature of the pattern. Hence, electron beam lithography (EBL) is necessary as photolithography can not treat components smaller than the wavelength of visible light. To avoid that the EBL-resist would curve for the long and thin patterns used here, an adhesion promoter was added before it. The adhesion promoter was TI-prime, and the EBL-resist was UV60-0.75(μm). Both these were spin-coated onto the chip and pre-baked. After exposure of the resist, the chip was post-exposure-baked to amplify the resist chemically. The lithography process was then concluded by developing the resist with MF-CD-26.

The pattern transfer was then done by inductively coupled plasma reactive ion etch (ICP-RIE) with the active gases silicon chloride ($SiCl_4$) and argon (Ar). Argon is used for ion milling. In other words, bombard the surface and physically remove one or multiple atoms. On the other hand, chlorine in $SiCl_4$ etches the layers horizontally while the silicon is used as a passive layer for the vertical surfaces. This

process result in sharp vertical walls. After dry etching, the resist is removed by remover 1165 and followed by O_2-plasma to ensure no resist residues are left. However, this is not enough to remove the adhesion promoter. Instead, etching with HF was necessary to remove TI-prime.

The GaAs layer is then etched to release the resonators. This is done by wet etching with citric acid and hydrogen peroxide used in a ratio of 5:1. These compounds are used as they result in a slow and controlled etch [58]. The sample is cleaned with DIW and IPA after the wet etch. It is essential during the wet etching to keep the chip in a liquid at all times. Otherwise, it is a risk that the resonators will collapse due to capillary forces. This is done by always keeping the sample in a Teflon holder filled with liquid. The sample is then dried with a critical point dryer (CPD). The resonators are then observed in scanning electron microscopy (SEM) to ensure they are fully suspended.

3.3 Characterization set-ups

The mechanical displacement of the fabricated resonators is detected by optical means, such that relevant mechanical and optical properties can be characterized.

3.3.1 Characterization of mechanical properties

Homodyne detection is an interferometric lock-in technique that, in its simplest form, consists of a coherent beam, a beamsplitter, and two photodetectors. The homodyne set-up used in this thesis is shown in Figure 3.4. The reference signal used in homodyne detection is denoted as a local oscillator (LO). The intensities measured at each of the two photodetector ($D1$ and $D2$) are:

$$I_{\mathrm{D1}} = |\alpha_{\mathrm{D1}}|^2 \quad \text{and} \quad I_{\mathrm{D2}} = |\alpha_{\mathrm{D2}}|^2 \tag{3.3}$$

α_{D1} and α_{D2} are the fluctuating amplitude of the light field at detectors 1 and 2, respectively, and are given by:

$$\begin{aligned} \alpha_{\mathrm{D1}}(t) &= \sqrt{\frac{1}{2}}\alpha_{\mathrm{lo}}(t) + \sqrt{\frac{1}{2}}\alpha_{\mathrm{s}}(t) \\ \alpha_{\mathrm{D2}}(t) &= \sqrt{\frac{1}{2}}\alpha_{\mathrm{lo}}(t) - \sqrt{\frac{1}{2}}\alpha_{\mathrm{s}}(t) \end{aligned} \tag{3.4}$$

where $\alpha_{\mathrm{s}}(t)$ and $\alpha_{\mathrm{lo}}(t)$ are the fluctuating amplitude from the LO and reflected arm. Both $\alpha_{\mathrm{s}}(t)$ and $\alpha_{\mathrm{lo}}(t)$ can be described by their respectively steady-state amplitude (α_{lo} and α_{s}) together with a fluctuating imaginary and real contribution,

$$\alpha_{\mathrm{s}}(t) = \alpha_{\mathrm{s}} + \delta X_{\mathrm{s}}(t) + i\delta Y_{\mathrm{s}}(t) \quad \text{and} \quad \alpha_{\mathrm{lo}}(t) = (\alpha_{\mathrm{lo}} + \delta X_{\mathrm{lo}}(t) + i\delta Y_{\mathrm{lo}}(t))e^{i\Phi}. \tag{3.5}$$

where the real contribution $\delta X(t)$ is the amplitude quadrature and the imaginary part is the phase quadrature $\delta Y(t)$. The amplitude and phase quadrature obey

Heisenberg's uncertainty and do not commute [59]. Hence, the phase and amplitude of the light wave cannot be measured with great accuracy simultaneously. Given that $|\alpha_{\mathrm{lo}}|^2 \gg |\alpha_{\mathrm{s}}|^2$, the difference in intensity between the two photodetectors can be calculated by substituting Equation 3.5 into Equation 3.3:

$$I(t) = I_{\mathrm{D1}}(t) - I_{\mathrm{D2}}(t) \approx \underbrace{2\cos(\Phi)\alpha_{\mathrm{lo}}\alpha_{\mathrm{s}}}_{\mathrm{DC}} + \underbrace{2\alpha_{\mathrm{lo}}[\cos(\Phi)\cdot\delta X_{\mathrm{s}}(t) + \sin(\Phi)\cdot\delta Y_{\mathrm{s}}(t)]}_{AC} \quad (3.6)$$

Thus, the difference in the intensity depends on a DC and an AC term. In the AC term, only one quadrature can be obtained with high accuracy at a given time. The quadrature of interest can be obtained by modulating the phase Φ. In this thesis, the phase shift and thus quadrature $\delta Y(t)$ is of interest. Hence, the phase is tuned to $\Phi = \pi/2$. The phase can be tuned in multiple ways. The set-up used here, illustrated in Figure 3.4, uses a proportional–integral–derivative controller (PID) and a phase modulator (PM) to tune the phase. The PID uses an error signal from the DC output to lock the phase to the set-point. The set-point is manually set to the maximum slope of the error signal, where the maximum sensitivity for the phase is obtained. The output voltage from the PID is then sent to a phase modulator. The phase modulator interacts with the LO-signal, keeping the set-point locked [12]. The outgoing RF-signal is then visualized in a noise power spectrum (NPS) by a Spectrum Analyzer.

A few measurements were also made for cryogenic temperatures to see if thermoelastic damping limited the quality factor. A similar set-up as the one shown in Figure 3.4 was then used, but with an additional cryostat.

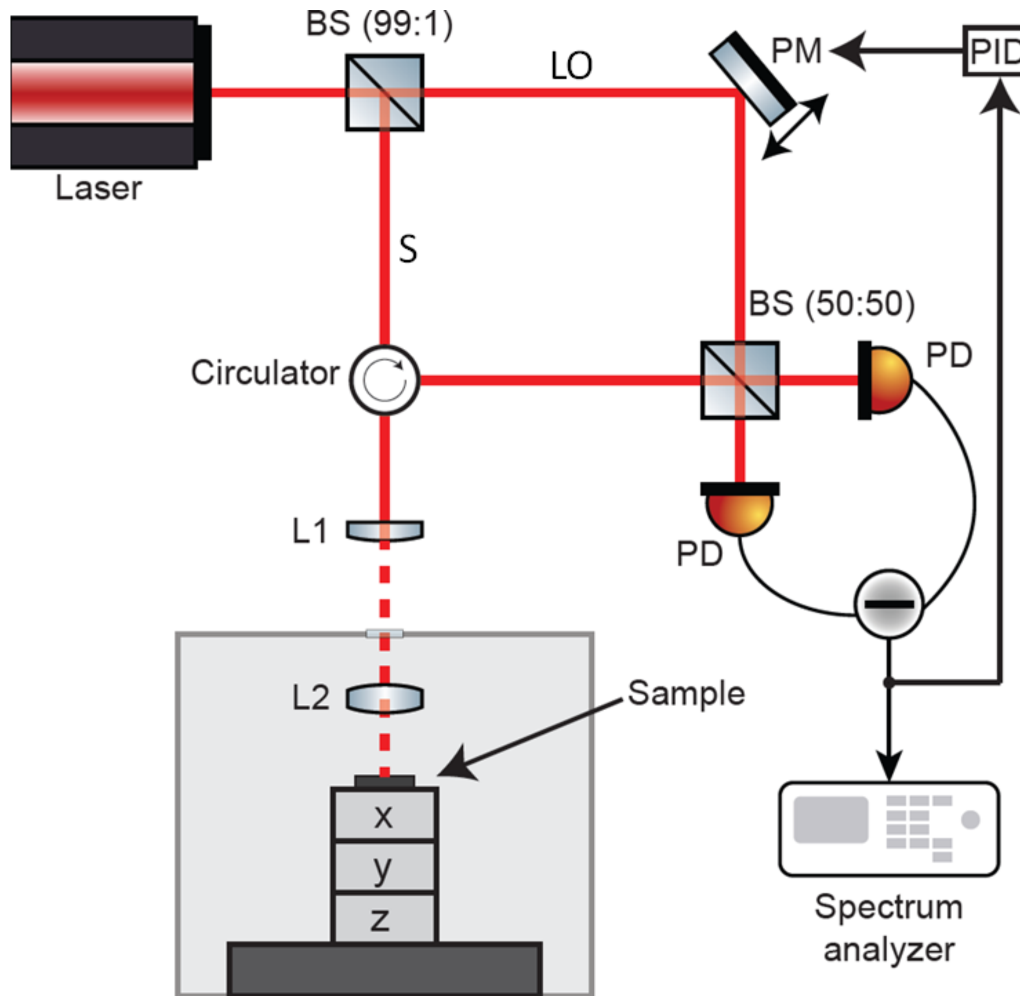

Figure 3.4: Schematic illustration of the homodyne used in this thesis. The laser beam, set to a wavelength of 1550 nm, is first divided into a LO and a signal arm with a ratio of 99:1. The weak laser beam in the signal arm is then transported through a circulator and a collimator. A lens then focuses the beam before it reaches the sample. The sample is in a chamber with a minimum pressure of 10^{-5} mbar. The sample reflects the beam, and the signal is transported back. It passes through the lens, collimator, and circulator again before it goes into a 50/50 beam splitter with the signal from the LO-arm, which the PID already modulates. The two signals are then detected by two photodetectors and visualized in a Spectrum analyzer. Courtesy of Sushanth Kini, Chalmers University of Technology.

3.3.1.1 Lorentzian fit

The resonance frequencies of the mechanical modes can directly be seen as the peaks in the NPS. An example of a NPS with a wide and a narrow frequency span is shown in Figure 3.5a and b, respectively. Γ, and thus Q, can be obtained by fitting the spectrum to the Lorentzian curve [13]:

$$f(\omega, \omega_m, \Gamma, c) = \frac{c}{\pi} \frac{\Gamma}{4(\omega - \omega_m)^2 + \Gamma^2} \tag{3.7}$$

where c is a fit parameter. This method is a time convenient and straightforward way to measure Q, but it has some limitations. For instance, the fit can only be evaluated if the bandwidth of the curve is larger than the smallest possible bandwidth of the spectrum analyzer.

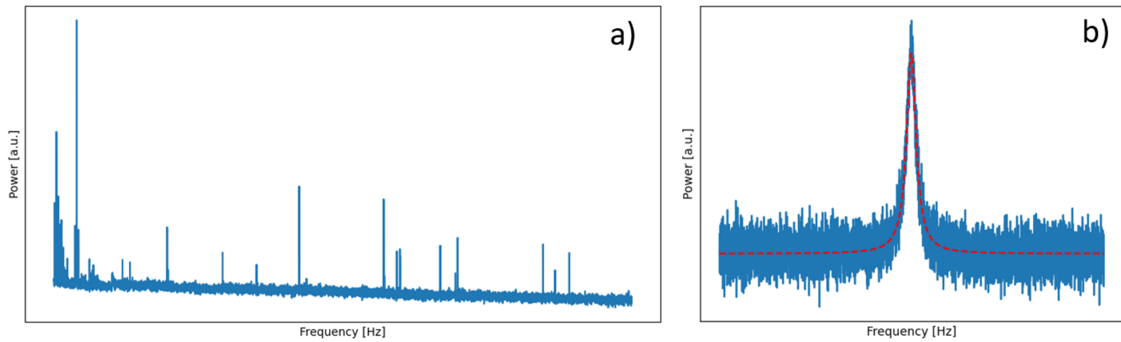

Figure 3.5: Example of NPS from a homodyne measurement for a large and a small frequency span in a) and b), respectively. In b) is a mechanical mode (blue) shown together with a Lorentzian curve fitted to it (red).

3.3.1.2 Ringdown

A more reliable way to determine Q is the *ringdown method*. At the start of the ringdown measurement, the mode is driven at its resonance frequency. As the actuation is stopped, the amplitude decays. The decay follows Equation 2.5. By taking the natural logarithm of the decay, Γ can be extracted from the linear function:

$$log(P(t)) = log(P_0) - \frac{\Gamma t}{2} \tag{3.8}$$

where $P(t)$ is the amplitude of the power at time t and P_0 is the amplitude at the beginning of the measurement. An example of a ringdown measurement together with its linear fitted curve is shown in Figure 3.6 [13].

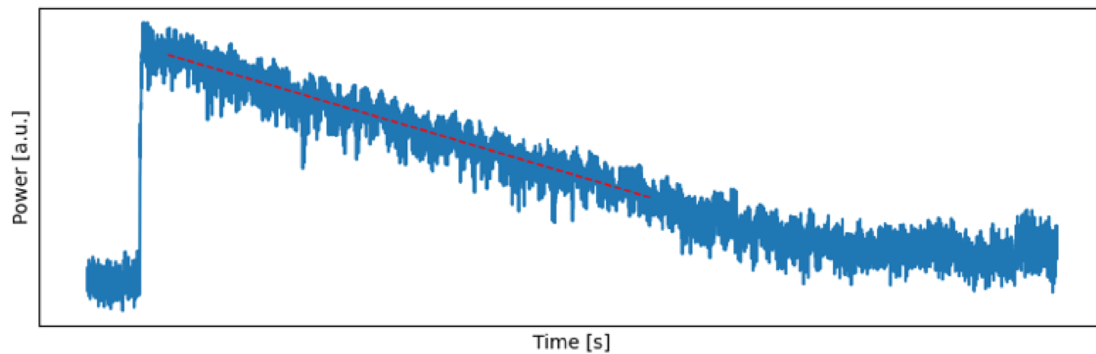

Figure 3.6: Example of a ringdown measurement (blue) together with a linear curve fitted to the measured data by Equation 3.8 (red).

3.3.2 Characterization of optical reflectivity

The reflectivity of the fabricated PhC is measured to verify that the optimized pattern and geometry of the PhC simulated in S^4 are accurate. The full set-up is illustrated in Figure 3.7. Here, a coherent light beam is produced by a tunable laser. The light is then transported to a collimator[1], transmitted through a linear polarizer and reflected by a Dichroic mirror[2]. The light is then rotated by a $\lambda/2$ wave plate. The light is then divided into two by a polarizing beam-splitter (PBS)[3]. The reflected beam is then detected by a photodetector, creating a reference signal. The transmitted beam is circularly polarized by a $\lambda/4$ wave plate[4]. The circular light is focused on the sample by a lens with a waist of 7.4 μm. The beam is either reflected or absorbed as it hits the sample. The reflected signal is transmitted back to the PBS where it is directed to another photodetector. The light signal from both photodetectors is then converted to a voltage signal and visualized in an oscilloscope. By tuning the wavelength, the reflectivity of the sample for multiple wavelengths can be collected. To ensure that the right device on the sample is measured, white light is used to image the sample.

To account for the optical loss which occurs within the set-up, a reference measurement is made to normalize the reflected signal of the resonator. Here, the reference measurement is made with a silver mirror with a known reflectivity R^{mirror}. The normalized reflectivity of a sample is then given by[57]:

$$R = \frac{V_{\text{reflected}}/V_{\text{reference}}}{V^{\text{mirror}}_{\text{reflected}}/V^{\text{mirror}}_{\text{reference}}} R^{\text{mirror}} \tag{3.9}$$

[1]A collimated beam has parallel oriented rays, which results in minimal scattering and loss during propagation

[2]A Dichroic mirror reflects light of certain wavelengths while the remaining light is transmitted through it.

[3]The horizontally polarized light is transmitted through the PBS while the vertically polarized light is reflected by it.

[4]$\lambda/4$ wave plate shits the linearized light by a quarter wave, resulting in circularly polarized light

where the voltage obtained from the reflected- and the reference signal power arm are $V_{\text{reflected}}$ and $V_{\text{reference}}$, respectively. On the other hand, $V_{\text{reflected}}^{\text{mirror}}$ is the reflected signal from the mirror and $V_{\text{reference}}^{\text{mirror}}$ is reference signal for the mirror.

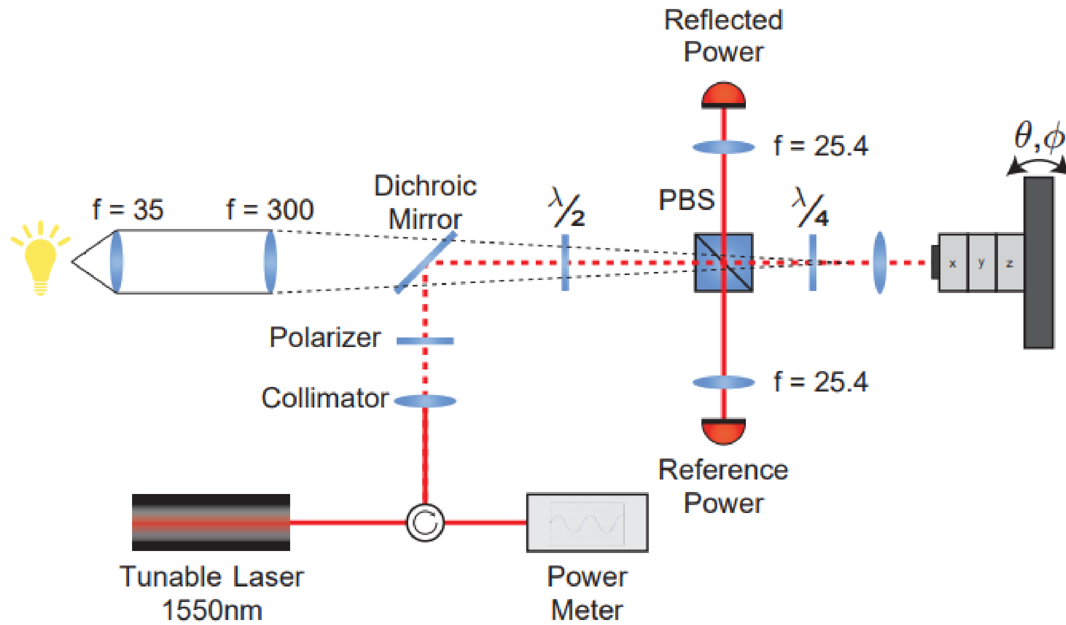

Figure 3.7: Schematic illustration of the set-up used to measure the reflectivity of PhCs. The light source is a tunable laser whose wavelength can be tuned between 1510-1620 nm. The laser beams penetrate a circulator, a collimator, and a polarizer in respective order before a Dichroic Mirror reflects it. Thereafter, it is transmitted through a $\lambda/2$ wave plate. The beam then reaches a PBS, where half of the signal is reflected and measured by a photodetector while the remaining light is transmitted through it. The transmitted beam continues through a $\lambda/4$ wave plate and then through a lens before it reaches the sample. The reflected signal propagates back to the PBS, where it is directed to a photodetector. A more detailed explanation of each component is described in the text. Courtesy of Sushanth Kini, Chalmers University of Technology.

4 Results

This chapter presents and discusses the design, fabrication, and characterization of micromechanical resonators made from InGaP. First, one-dimensional strings are treated, which are designed and fabricated to obtain the material's intrinsic properties — σ and Q_{int}. The reaming part of this chapter treats two-dimensional trampolines, where the design of these is first optimized to minimize mechanical dissipation. The mechanically optimized trampolines are then fabricated and characterized to investigate the limiting mechanical loss mechanisms. Lastly, the optimization of the PhC is discussed and implemented to enhance the optical read-out.

4.1 1D resonators - Strings

The intrinsic properties were extracted from the material by utilizing analytical modelling presented in Section 2 applied to the fabricated InGaP strings. The first step to realizing the string resonators was to choose a proper design for them.

4.1.1 Design of strings

The frequencies of interest were between 100 kHz to 5 MHz. Equation 2.32 was used to see which lengths of strings had a fundamental mode within this span. The stress used for this calculation was set to 500 MPa. This stress is the epitaxially grown stress based on the gallium content in $\text{In}_{1-x}\text{Ga}_x\text{P}$, which here is x=0.58. The result is plotted in Figure 4.1a. It can be seen that strings with lengths between 30-150 μm have a fundamental mode within the frequency span of interest. Hence, the fabricated strings had the lengths: 20, 30, 45, 65, 90, 120, and 155 μm, with four different widths: 0.2, 0.5, 1, and 2 μm. Furthermore, each set of strings was fabricated for three different crystal directions since InGaP is anisotropic and the stress varies along different crystal axes. The mask including all of these strings is shown in Figure 4.1b.

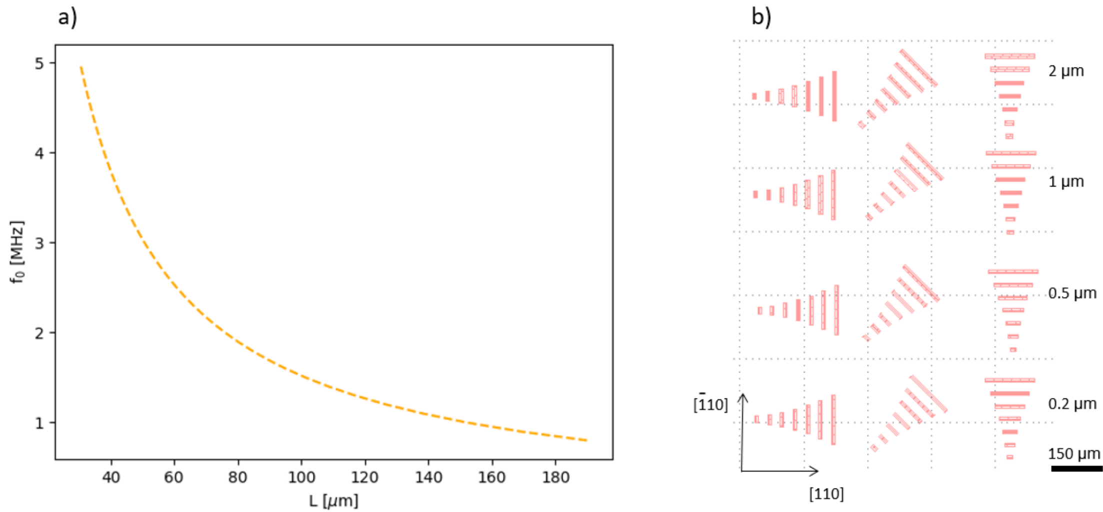

Figure 4.1: Design of the strings. a) shows a graph illustrating which length the string with a stress of 500 MPa must have to obtain a fundamental frequency between 100kHz-5MHz. b) shows the mask used for the fabricated strings.

4.1.2 Mechanical characterization of strings

The strings were observed in optical- and scanning electron microscope after fabrication, to ensure that they were suspended and were free from residues. Figure 4.2 shows images of fabricated string resonators. Additional SEM images for strings with different widths are shown in Figure 4.3. It can be seen from all SEM images in Figure 4.2 and 4.3 that all strings, independent of width, are suspended and are thus free to vibrate.

It can be seen from Figure 4.2 that the etch rate of GaAs was anisotropic. From InLens SEM images, the etch rate was determined to be 0.3 and 0.5 μm/min along the [$\bar{1}$10] and [010] direction, respectively. This is faster then the etch rate reported in literature (0.2 μm) for the same ratio of citric acid and hydrogen peroxide [58]. This resulted in a large under-etch for the [$\bar{1}$10]-strings, which can explain the damaged under-etch for the strings in Figure 4.2c.

The characterization of the mechanical properties of these strings was performed and an example of a NPS of a string is shown in Figure 4.4a, along with the mode shapes for each peak obtained from COMSOL. The peak of interest here is the fundamental mode. A compilation with all fundamental frequencies for all strings along the [$\bar{1}$10] is shown in Figure 4.4b. Here, it can be seen that the frequency increases with an decreased length of the string, which agrees with Equation 2.33.

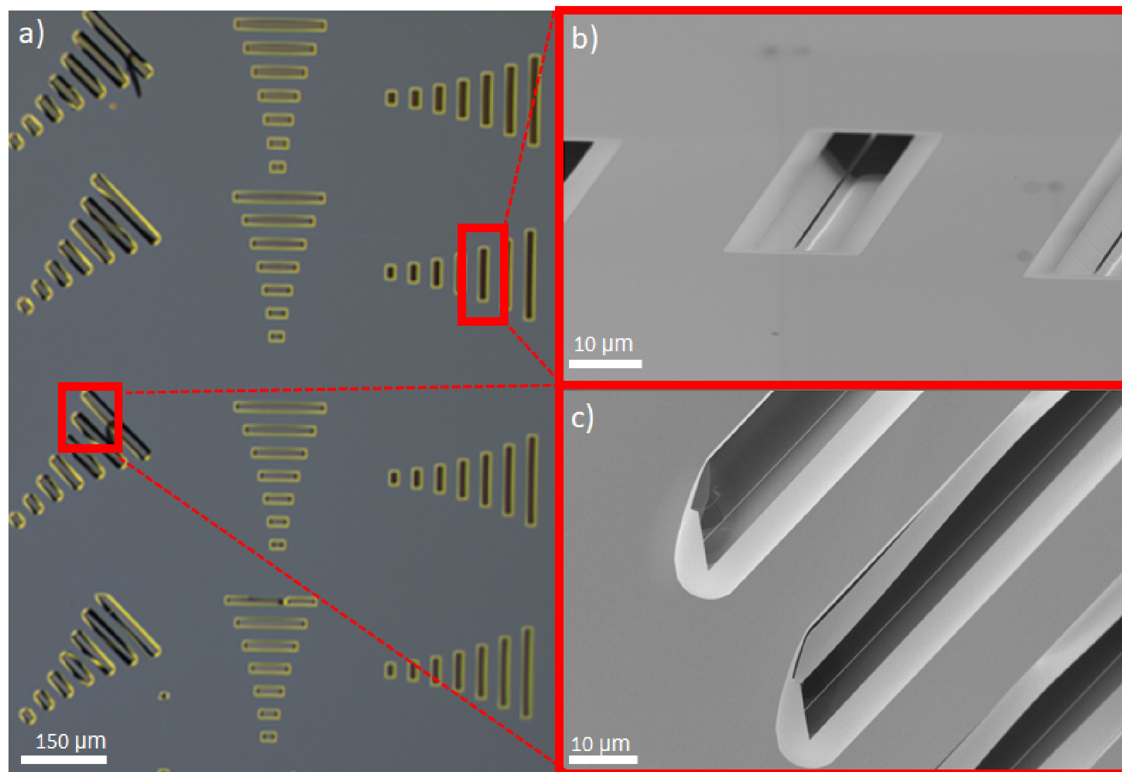

Figure 4.2: Image of fabricated suspended strings. a) shows multiple strings with different directions, length and widths taken with an optical microscope. b) and c) are SEM pictures of a string along the $[\bar{1}10]$ and [010] directions, respectively.

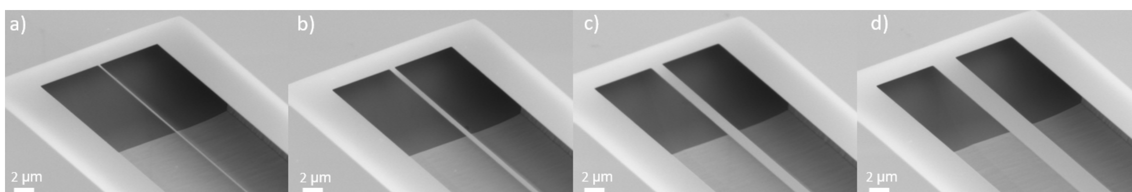

Figure 4.3: .
]Image of strings with different width oriented along [110]. The width of the strings are 0.2, 0.5, 1, and 2 μm for a)-d), respectively.

The measured fundamental frequencies were used with Equation 2.33 to extract the intrinsic stress in the InGaP layer and the result is presented in Figure 4.5. The measured frequencies for strings along $[\bar{1}10]$ with a width of 0.2 μm are shown in Figure 4.5a, together with the analytical model presented by Equation 2.33. This procedure was performed for each width and each direction and the result is shown in Figure 4.5b. The obtained stress is anisotropic; this is a result of the anisotropic Young's modulus. The same behaviour has also been reported in [40].

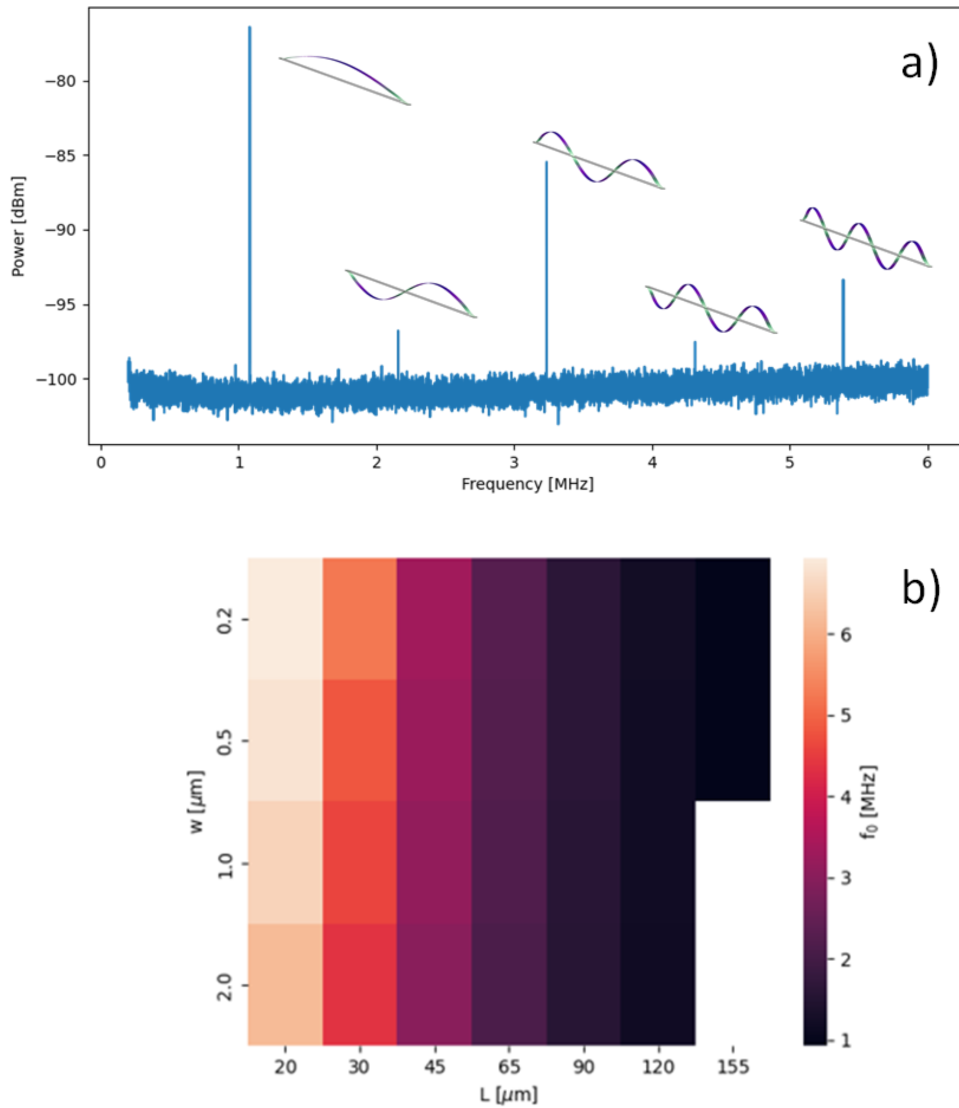

Figure 4.4: Measured frequency dependence of strings. In a) is an NPS obtained for a string together with images from COMSOL showing each mode of the peak. b) shows the measured fundamental frequency for multiple strings with different length and widths. All these strings are along $[\bar{1}10]$.

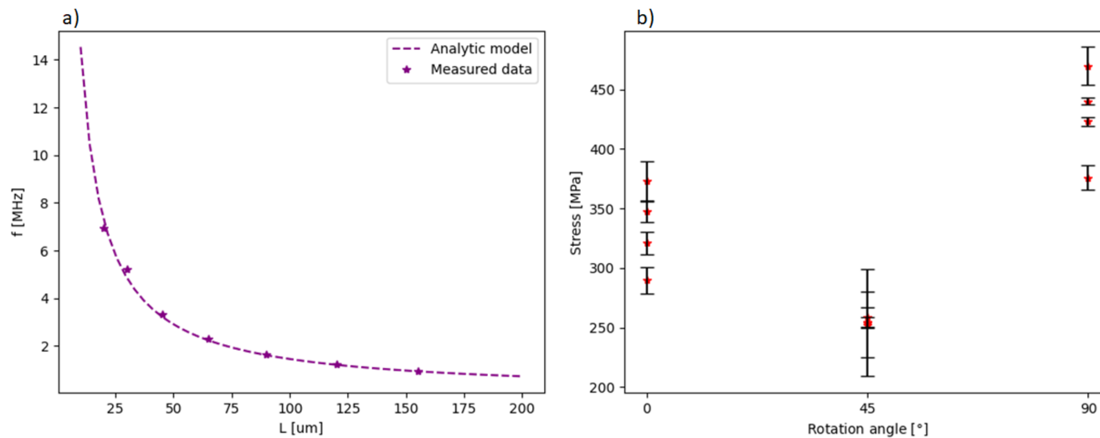

Figure 4.5: Extraction of stress from strings. In a) is measured data for multiple string with varying lengths shown together with a curve which is fitted to it based on Equation 2.33. Here, the width (0.2 μm) and direction ($[\bar{1}10]$) for the strings are fixed. Extraction of the stress was made for different widths and crystal direction and the result is shown in b). The rotation angle is illustrated in 3.1b.

The quality factors for the fundamental modes were extracted for the same strings. The effect the width and the length of the strings have on the Q for the fundamental mode is shown in Figure 4.6a for vertical strings. Longer strings result in a enhanced quality factor, which is a sign that the string's quality factor might be limited by clamping loss, based on Equation 2.24. It can also be limited by TED or gas damping. However, gas damping can be ruled out as a possible damping mechanics at the operating pressure ($\sim 10^{-5}$ mbar) due to the result shown in Figure 4.6b. Here, the analytical calculation of Q_{gas} from Equation 2.26 is shown together with the measured Q for the same string at increased pressures. The Q for the measured data is not linear dependent and follows not the analytical Q_{gas} for pressures less than $5 \cdot 10^{-2}$ mbar. Hence, the system is limited by gas damping for $P > 5 \cdot 10^{-2}$ mbar but not for lower pressures.

The intrinsic quality factor for the material was then determined by fitting the measured Q for different lengths of strings together with the experimentally measured stress to Equation 2.35. This is done for strings in the vertical and horizontal direction in Figure 4.7 a and b, respectively. Q_{int} is here anisotropic and showed to be 5700 ± 1000 for the vertical strings and 7900 ± 1700 for the horizontal strings. These values for Q_{int} are larger than Q_{int} for InGaP obtained by other research groups, 2400 [27]. However, Q_{int} depends on the growth conditions which can explain the difference. Since Q_{int} is a measure of the number of defects in a material, it would mean that the growth used in this thesis has few defects [27]. These defects can also occur later if the material is oxidized. Furthermore, the gallium content for InGaP was also different in the two works and could explain the difference. The intrinsic Q_{int} obtained here is also in the same range as other materials such as Si_3N_4, see Table 0.2.

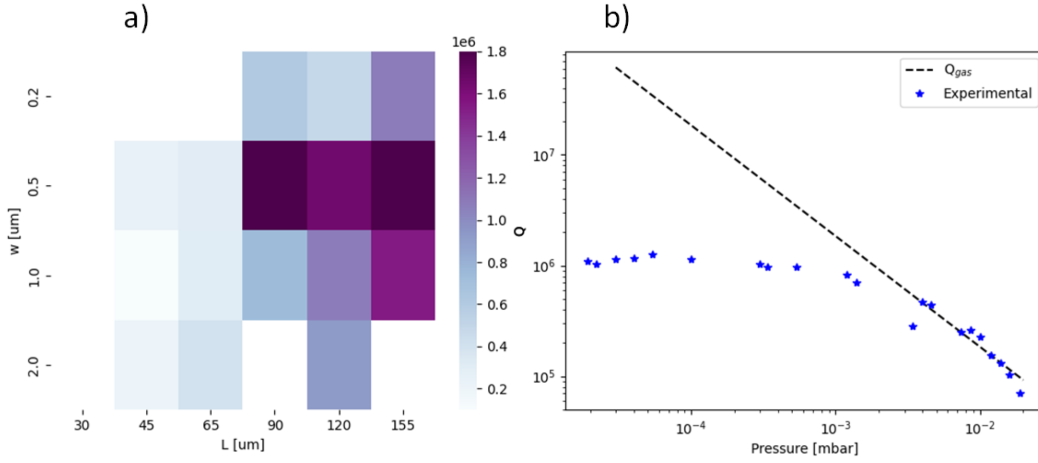

Figure 4.6: Measured Q for strings. In a) is Q shown for multiple widths and lengths for strings along $[\bar{1}10]$. Missing values are shown as white squares. b) shows measured values for a string for varying surrounding pressures together with analytical calculated Q_{gas} from Equation 2.26.

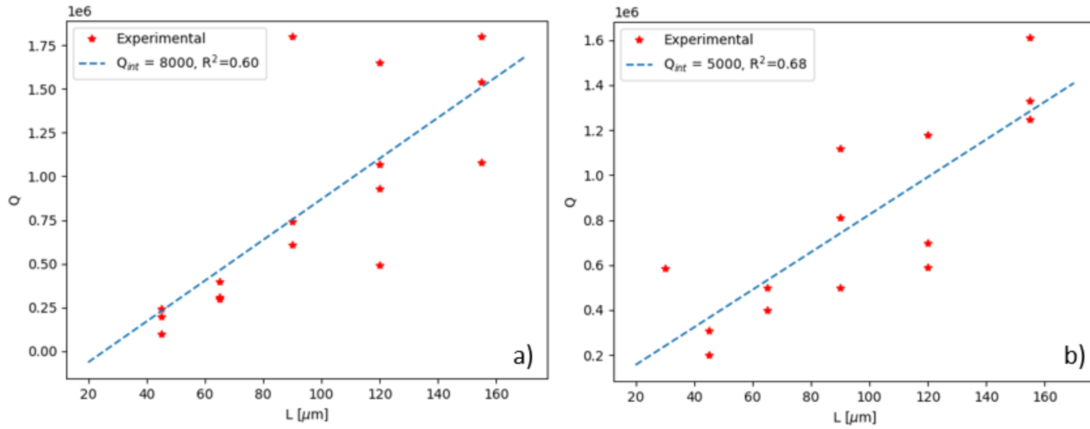

Figure 4.7: Extraction of Q_{int} from Equation 2.37 and measured Q from strings with varying lengths. a) shows the extraction made for vertical strings while it is done for horizontal strings in b).

4.2 Trampoline-type micromechanical resonators

This section presents the results obtained for the two-dimensional trampoline resonators. Here, the design of the trampolines was split into two parts. First, the resonator was designed to enhance Q, while the second part focuses on enhancing the reflectivity by alternating the design of a PhC.

4.2.1 Optimizing the design for trampolines to enhance mechanical Q

It was shown in Section 2.1 that a high sensitivity would be obtained for resonators with large Q. Also, in the context of quantum experiments, a large Q is pivotal to ensure long coherent times of quantum states. Thus, it is essential to get a large Q and a high frequency simultaneously.

The stress used for the simulation is based on the stress given by the growth of the InGaP layer on the GaAs-wafer. Furthermore, only a fourth of a trampoline (and PML) together with a symmetry condition to simulate the full structure shown in Figure 4.8 was used for the simulations. In the same figure, a) shows the PML and b) is a magnified picture of the trampoline located in the center of the PML. Lastly, remember that the COMSOL simulations made here only consider the dissipation due to clamping.

The geometry of the trampoline was optimized to enhance Q by varying the parameters r_{out}, r_{in}, a_{window}, a_{pad} and w_{t}, all of which are shown in Figure 4.10e. One parameter was probed at a time, and the remaining parameters were set to a constant value. The fixed values are shown in Table 4.1. Each sweep was done in two directions; one where the tethers were along the $[\bar{1}10]$ axis and another with a rotation of 45° around the z-axis, see Figure 4.9. The simulated fundamental mode's frequency and Q for the different parameter-sweeps for the first mentioned direction is shown in Figure 4.10.

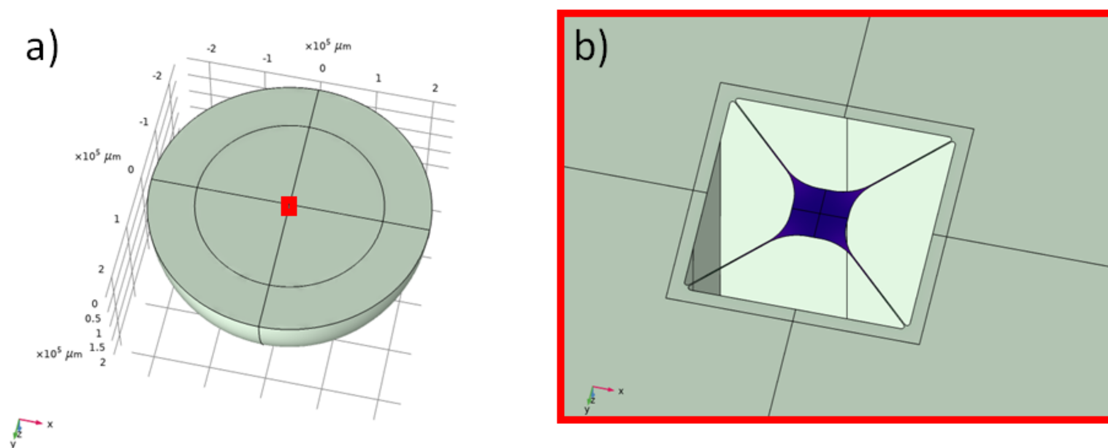

Figure 4.8: Geometry of the trampoline resonators used for COMSOL simulations. a) shows the PML with the trampolines located in the middle and b) shows a close up of the trampolines.

r_{out}	r_{in}	a_{window}	a_{pad}	w_{t}
20 μm	60 μm	700 μm	100 μm	5 μm

Table 4.1: Reference values of the parameters for COMSOL simulations.

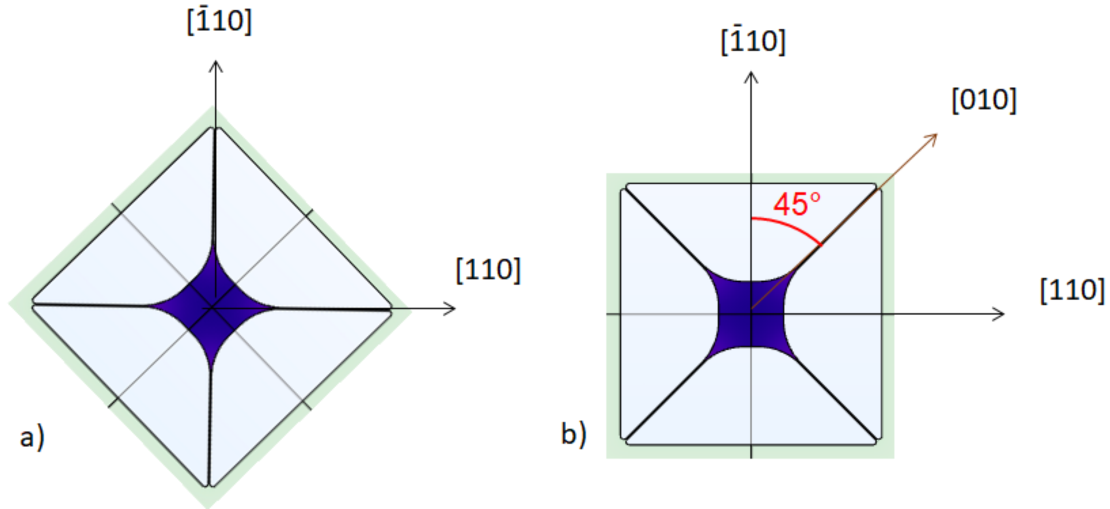

Figure 4.9: Orientation for trampoline in simulations. a) and b) shows a trampoline with 0° and 45° rotation, respectively.

The mass of the micromechanical resonator significantly increases as the size of the pad increases. According to Equation 2.1, this increase in mass results in a decreased frequency, which is also seen in the simulations shown in Figure 4.10d. Furthermore, the frequency can also decrease due to a reduced spring constant. This occurs, for instance, for longer and less rigid resonators, which are also observed in the simulations shown in Figure 4.10c.

A similar trend as the analytical formula for clamping loss of a string explained by Equation 2.24 can also be seen for the simulations; Q increases for longer and thinner strings, i.e. tethers. The tethers can be longer by increasing the window or decreasing the pad size. For larger a_{window}, in Figure 4.10c, and narrower w_{t}, in Figure 4.10b, a significant increase of Q between data points can be observed. For both parameters, Q increases with at least a factor of 10 between their minimum and maximum. a_{pad} also affects Q but not to the same extent. Based on the same argument as before, Q should decrease for larger a_{pad} as these result in shorter tethers. However, this is only true for pads larger than 225 μm in Figure 4.10. For $a_{\text{pad}} > 225\mu\text{m}$ Q decreases as a_{pad} decreases.

There is no significant change in the frequency as r_{in} varies, shown in Figure 4.10e. Here, the quality factor changes less than ±20%. Furthermore, r_{in} has no significant impact on the resonance frequency. On the other hand, r_{out} affects both the frequency of the fundamental mode and its Q. The frequency follows the same trend that also has been reported in other works [5], [16]; the frequency increases for larger clamping points. Furthermore, the quality factor decreases for increased values of r_{out}. This contradicts the trampolines presented in [5], where a widening of the clamping points resulted in soft clamping and thus decreased Q. For the simulations made in this thesis, soft clamping could also be observed for wider r_{out} by taking the cross-section of the mode shape along a tether, see Figure 4.11a. The simulated mode shapes are shown in Figure 4.11b for trampolines with r_{out} of 5, 20,

and 40 μm. Here, the bending near the attachment points decreases for resonators with wider clamping points. However, this does not explain why the Q obtained here decreases for larger clamping points. The quality factor instead follows the same trend as for strings with widening clamping points presented in [16] and [60]. The reason why it increases for smaller regions could be due to strain engineering, where the strain is delocalized from the bulk to the small clamping points [60]. Furthermore, the large area of the clamping for larger r_{out} enables larger radiation from the resonator to the supporting structures which also can be the reason for the decreasing Q.

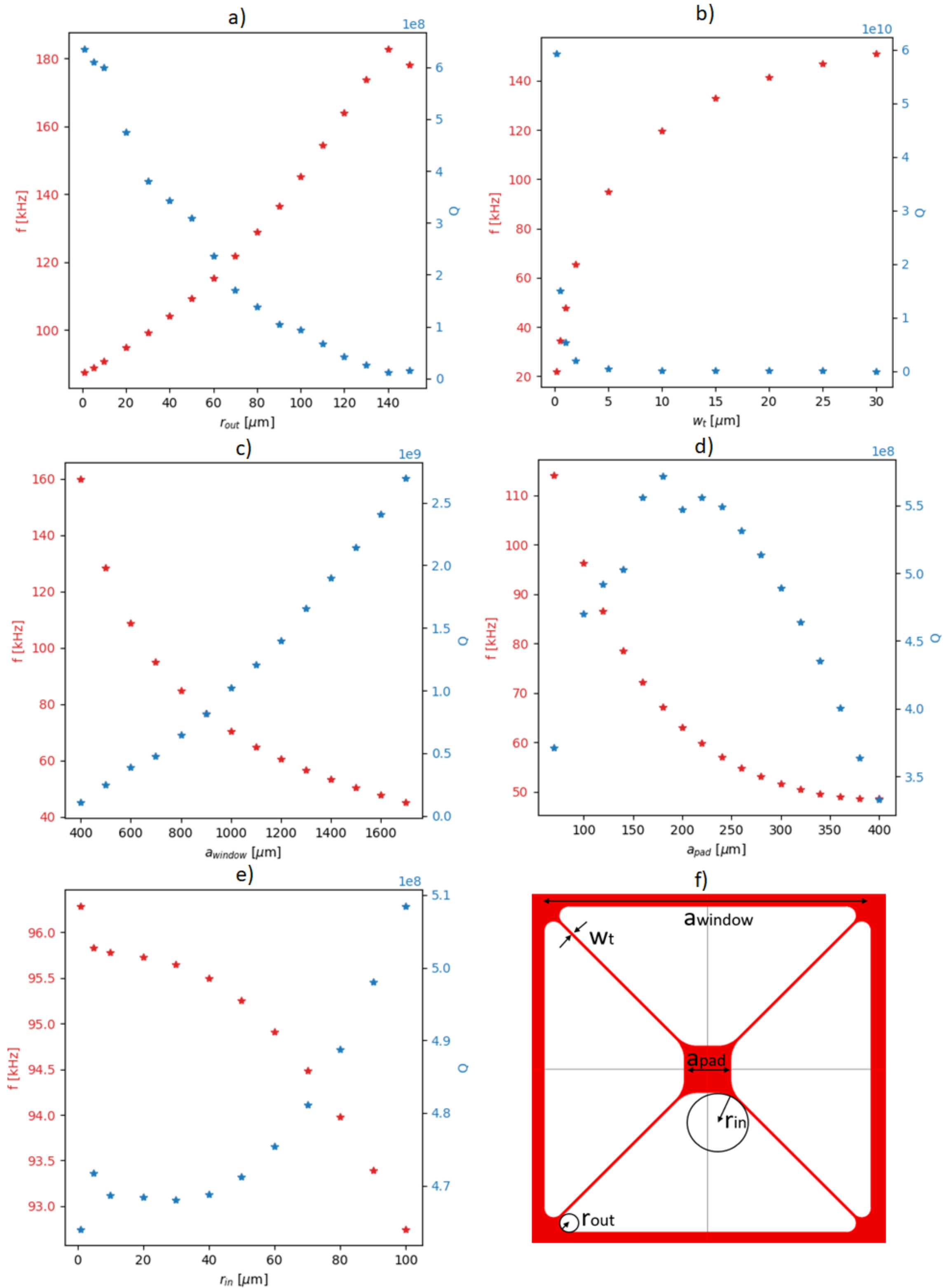

Figure 4.10: Result of the quality factor and the fundamental frequency from simulations for different parameter-sweeps. a)-e) shows the sweep of the parameter r_{out}, w_{t},a_{window}, a_{pad} and r_{in}, respectively. f) shows the variables which are varied in the simulations.

As mentioned earlier, the simulations were done for two different orientations. The simulations from the two directions are compared by evaluating $Q \cdot f$ for them. The result is shown in Figure 4.12. $Q \cdot f$ is used as a comparison as it was shown to be of considerable interest for quantum experiments. The same trends can be seen in both directions for all sweeps, except for r_{in}. Furthermore, the simulated $Q \cdot f$ for trampolines which are rotated by 45° are always higher than the trampolines which are not rotated. Possible due to higher stress in the tethers in this direction based on the result shown in Figure 2.6. The mechanical quality factor also have the largest impact on $Q \cdot f$ for these simulations. However, one interesting difference is for a_{pad}, where the maximum for $Q \cdot f$ occurs at $a_{\text{pad}} = 100\mu\text{m}$ while it occurs at $a_{\text{pad}} = 175\mu\text{m}$ for Q.

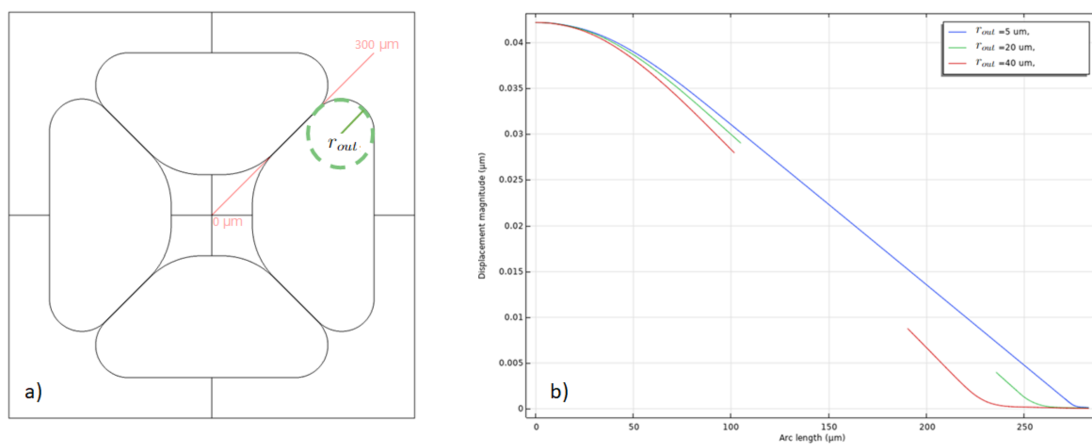

Figure 4.11: Investigation of clamping for different r_{out}. The red line in a) with origin in the center of the trampoline illustrates the cross-section used to obtained the mode shapes shown in b). In b) is the mode shape of a trampoline with $r_{\text{out}} =$ 5, 20 and 40 μm shown.

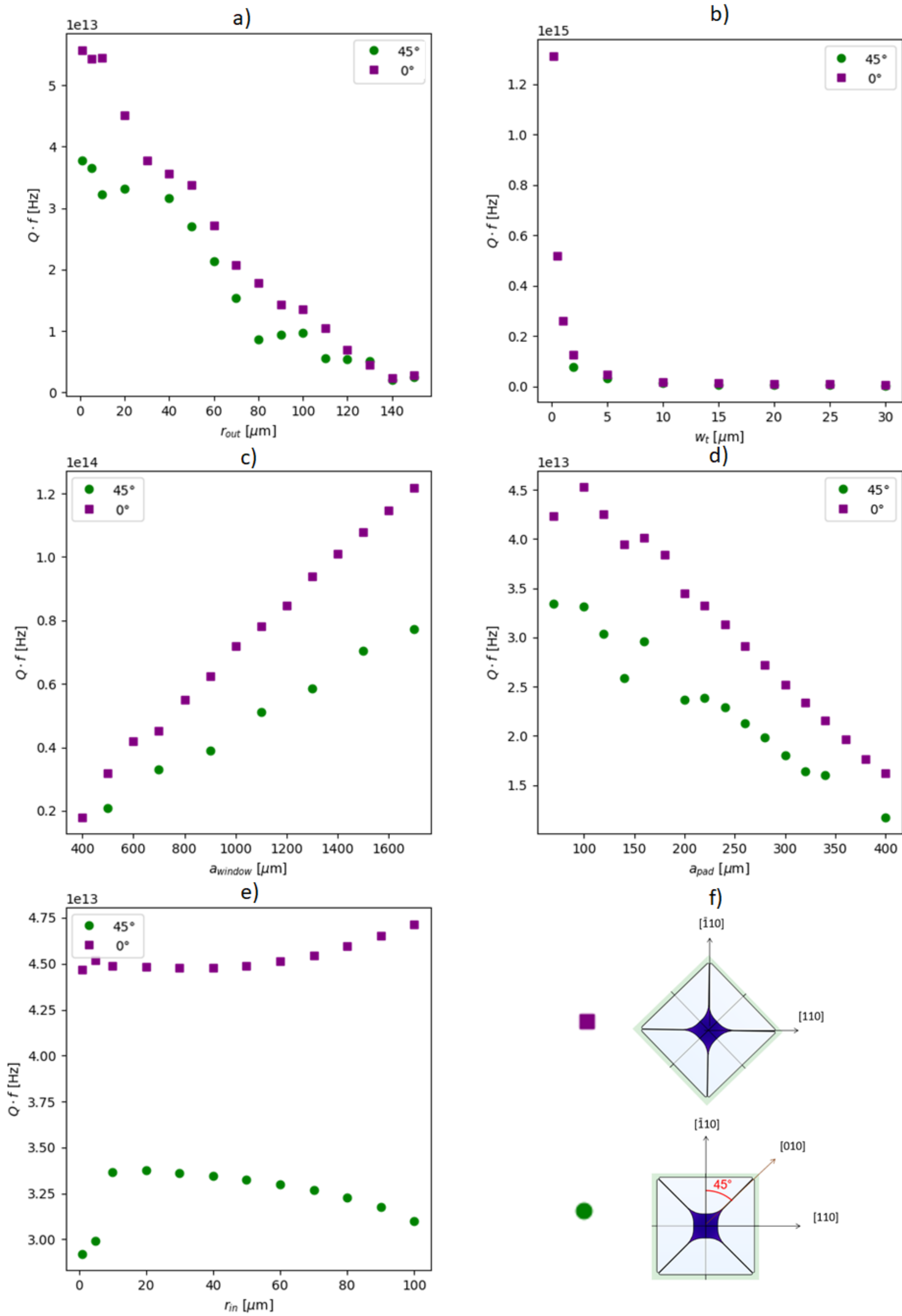

Figure 4.12: The directions influence on $Q \cdot f$ for simulations. a)-e) shows the sweep of the parameter r_{out}, w_{t},a_{window}, a_{pad} and r_{in}, respectively. f) shows the different orientations for the trampolines.

4.2.2 Mechanical characterization of trampolines

Several trampolines were then fabricated based on the result obtained from the simulations. The design for the PhC used here is discussed in more detail in Section 4.2.3. For these trampolines, the width and length of the tethers were varied, while the remaining parameters were set to be constant. The tethers' width and length were here changed as they have the strongest impact on Q. Further, the fabrication can also limit these as thinner and longer strings are harder to fabricate. Table 4.2 shows the parameters' range and fixed values. The mask for this is shown in Figure 4.13a. It was also shown in the simulations that a larger $Q \cdot f$ was obtained for trampolines with tethers oriented parallel to the $[\bar{1}10]$ direction. However, this was not implemented here in order to save space on the chip which was diced along $[\bar{1}10]$.

Parameter	Value
r_{out} [μm]	5
r_{in} [μm]	100
a_{pad} [μm]	100
w_{t} [μm]	[0.5,1,2]
a_{window} [μm]	[400, 600, 800]
D_{Mirror} [μm]	100
a_{PhC} [nm]	1323
r_{PhC} [nm]	550

Table 4.2: The parameters used for the first generation of fabricated trampolines.

In the first generation of fabricated trampolines, all trampolines broke at the end of the PhC, which can be seen in Figure 4.13 b and c, which was probably due to immense stress in these regions. To avoid this for the next generation of trampolines, D_{Mirror} was increased. The values for the different parameters for the second generation of trampolines are shown in Table 4.3, and an optical image of the result is shown in Figure 4.14.

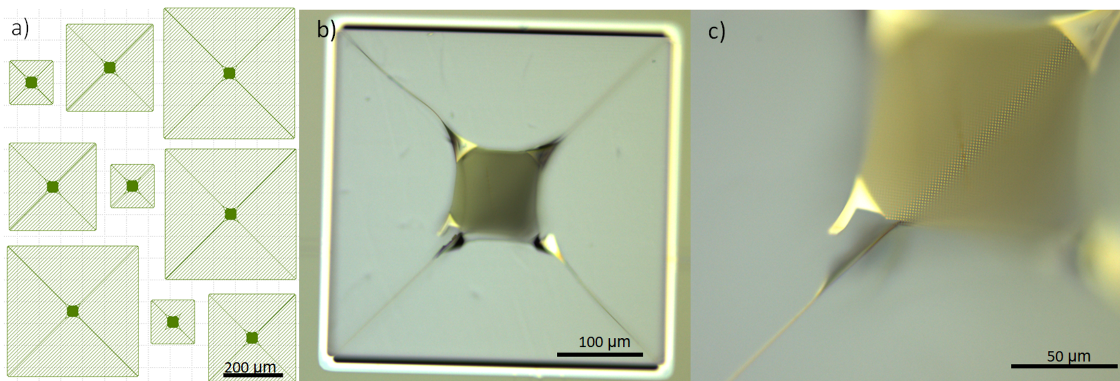

Figure 4.13: First fabrication of optimized trampolines. The mask used for the fabrication is shown in a). b) and c) are optical microscope images of one fabricated trampoline which broke at the end of the PhC. c) is here a magnified image of b).

r_{out} [μm]	5
r_{in} [μm]	100
a_{pad} [μm]	100
w_{t} [μm]	[0.5,1,2]
a_{window} [μm]	400
D_{Mirror} [μm]	[120 ,140, 160, 180, 200]
a_{PhC} [nm]	1323]
r_{PhC} [nm]	550

Table 4.3: The parameters used for the second generation of fabricated trampolines.

In Figure 4.14, multiple trampolines with all different w_{t} are intact and suspended for D_{Mirror} equal to 160 or 180 μm. These trampolines' fundamental frequency and Q were then characterized. An example of a NPS for one trampoline is shown in Figure 4.15.

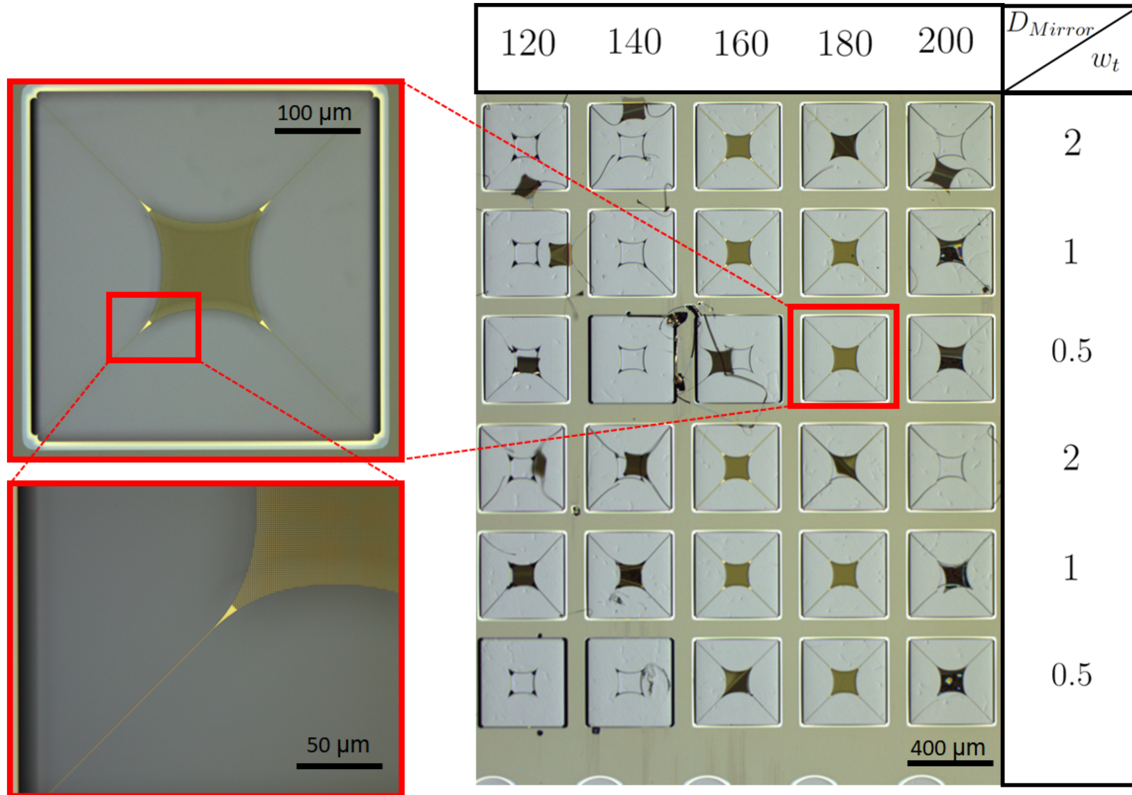

Figure 4.14: Optical images of the result from the second fabrication of optimized trampolines.

The COMSOL simulations showed trampolines with wider tethers resulted in higher frequencies. This statement is still valid for the fabricated resonators, as shown in Figure 4.16a for data measured at 300 K and 5 K. The same figure shows the simulated values for these devices for comparison. The measured and simulated

eigenfrequency matches well. However, this cannot be said for the Q plotted in Figure 4.16b. Here are two critical points worth noticing. First, the simulated quality factors are much larger than the measured ones. Secondly, Q for the measured resonators does not increase as the width of the tethers decreases, which does not agree with the simulated values. Instead, Q is relatively constant for all the widths measured at the same temperature. These two factors indicate that the trampolines are not limited by clamping loss but by another damping mechanism, such as TED, gas, or intrinsic dissipation.

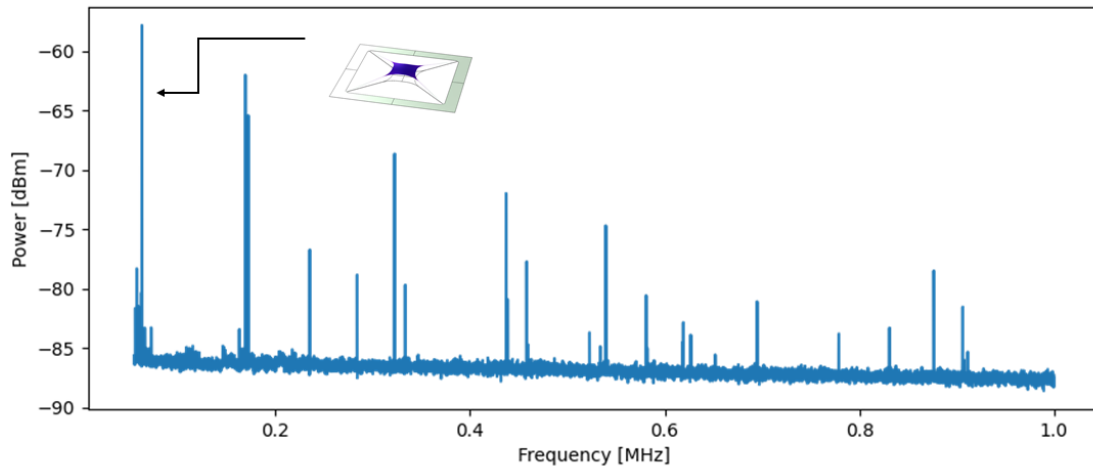

Figure 4.15: NPS for optimized trampolines with $w_t = 0.5\mu$m together with an insert of the COSMOL image of the fundamental mode and which peak it corresponds to.

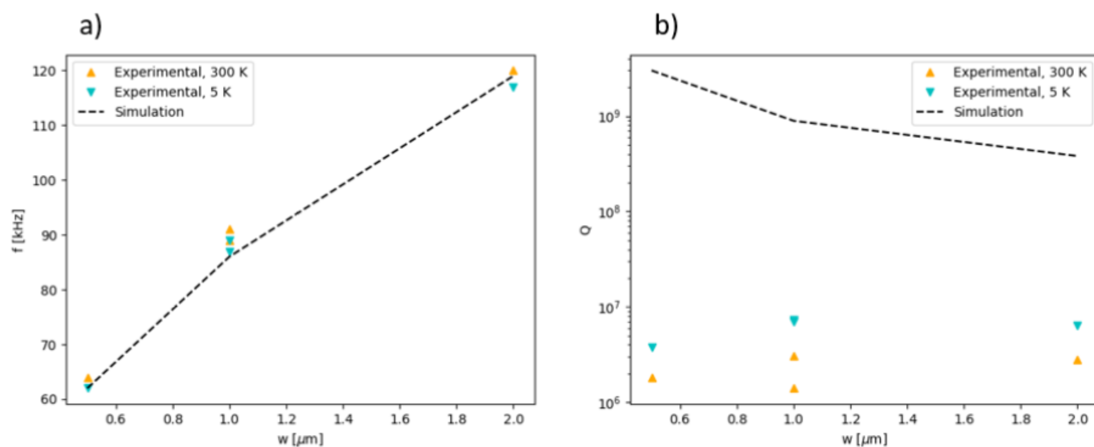

Figure 4.16: w_t impact of the mechanical properties. a) shows how the measured and simulated fundamental frequency depend on w_t, while b) shows how Q depends on w_t. The stress used for the simulations was 500 MPa.

The same procedure to measure gas damping for strings was then done for trampolines and the result is shown in Figure 4.17 together with the analytical calculation

for Q_{gas} based on Equation 2.26. It can be seen that the resonator is heavily gas damped for larger pressures ($P > 2 \cdot 10^{-4}$ mbar) as it follows the analytical model very well. For small pressures, the quality factor of the trampolines are still influenced by gas damping, but not to the same extent.

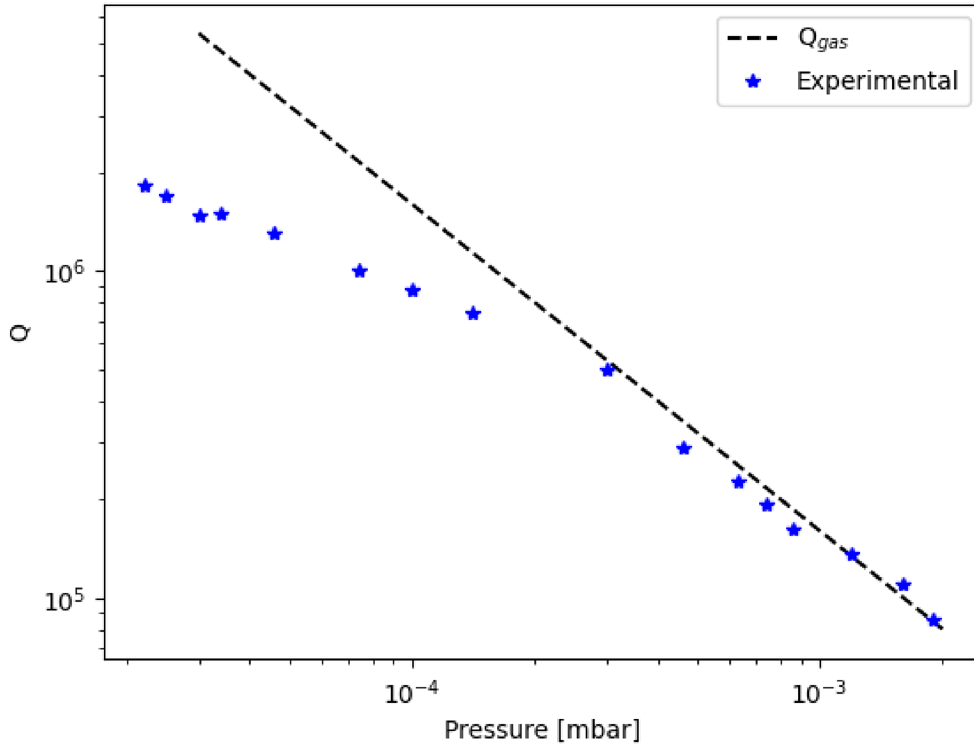

Figure 4.17: Pressure dependence of Q for the fundamental mode of a trampoline resonator and analytical model of Q_{gas} from Equation 4.17

One of the resonators was then measured at different temperatures in another chamber to investigate two phenomena. Firstly, it was used to see if it could reach lower pressures by changing the temperature and thus not be limited by gas damping. Secondly, it was also interesting to investigate if TED would be present. The result is shown in Figure 4.18. In an ideal scenario, the pressure would be kept constant during the temperature sweep. However, this was not possible for all measurements done here. The pressure varied between $10^{-3} - 10^{-5}$ mbar for the datapoints denoted 'i' in Figure 4.18, and the pressure was relatively constant at $\sim 10^{-5}$ mbar for the points marked as 'ii'. Here, Q increases as the temperature decrease for higher temperatures. This signifies that TED might be present. However, this might not be entirely true in this case as the pressure also increases for these measurements and has a starting point at $\sim 10^{-3}$ mbar and decreases to at least $\sim 10^{-5}$ mbar. Furthermore, the analytical Q_{TED} based on Equation 2.20 show a $Q_{\text{TED}} \approx 10^8$ at room temperature and even higher for lower temperatures. This result indicates that the measured decrease in Q is not a result of TED. However, it is essential to remember that this model is formulated for a string. Lastly, for low temperatures

all the measured Q are larger than $5 \cdot 10^6$ independently of the temperature. Thus, TED is at least not the limiting factor for temperatures below 80 K. However, further investigation must be done to say with certainty that TED does not limit the resonators at room temperature. In the future, it would be interesting to simulate TED for complicated geometries with COMSOL.

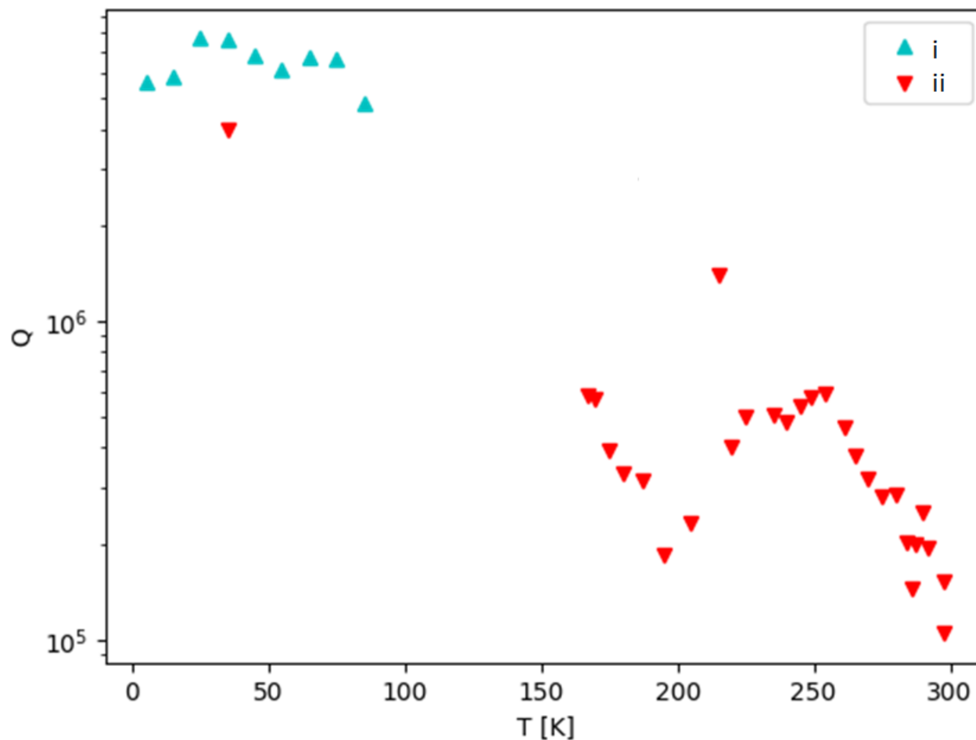

Figure 4.18: Q measured at different temperatures. The pressure varied between $10^{-3} - 10^{-5}$ mbar.

4.2.3 Design of PhC

A single planar wave was used for the first simulations in S[4]. These computations were fast and used to get an idea of which values of a_{PhC} and r_{PhC} that would result in a high reflectivity at $\lambda = 1550$ nm. For these simulations, the radius and the lattice constant were varied between $0.1\lambda \geq r_{\text{PhC}} \geq 0.5\lambda$ and $0.6\lambda \geq a_{\text{PhC}} \geq 1.1\lambda$, while the wavelength was fixed. The result is shown in Figure 4.19a. It can be seen that several regions have large reflectivity. A magnified picture of a region with a large reflectivity can be seen in Figure 4.19b. Within this region, $a_{\text{PhC}} = 1323$ nm and $r_{\text{PhC}} = 550$ nm were chosen as a guideline for the remaining simulations.

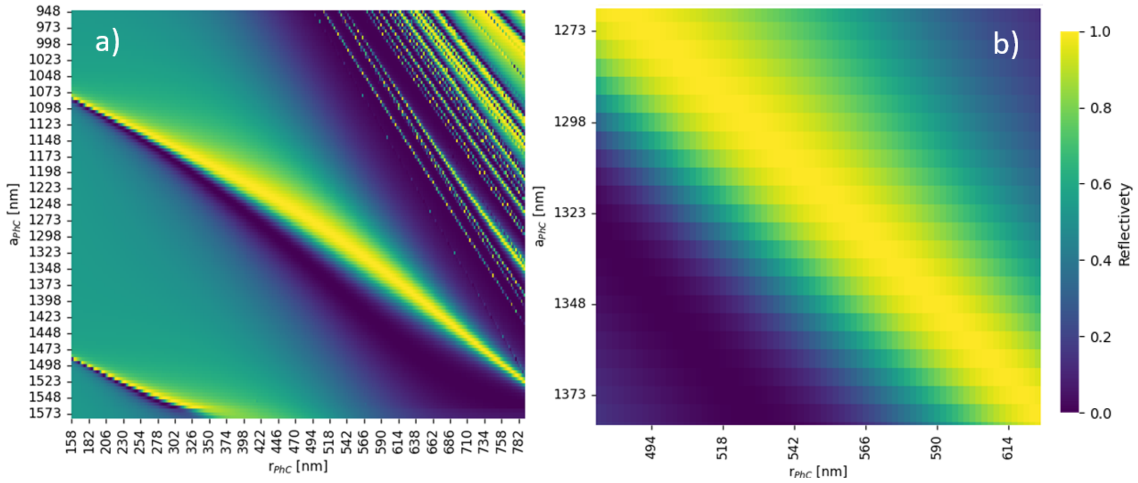

Figure 4.19: Simulated reflectivity of PhC at $\lambda = 1550$ nm with respect to a_{PhC} and r_{PhC}. In a) is $0.1\lambda \geq r_{\text{PhC}} \geq 0.5\lambda$ and $0.6\lambda \geq a_{\text{PhC}} \geq 1.1\lambda$, while a magnified plot for values around $a_{\text{PhC}} \sim 1300$ nm and $r_{\text{PhC}} \sim 500$ nm is shown in b).

The wavelength was then varied between 1400-1700 nm for these fixed values for a_{PhC} and r_{PhC} to see the reflectivity was affected. The result is shown in Figure 4.20a. Here, the reflectivity peak occurs at 1575 nm. The same simulation was then done for multiple r_{PhC} to see if it influenced the location of the peak. The result is shown in Figure 4.20a, where it can be seen that the reflectivity peak drifts to larger wavelengths as r_{PhC} decreases.

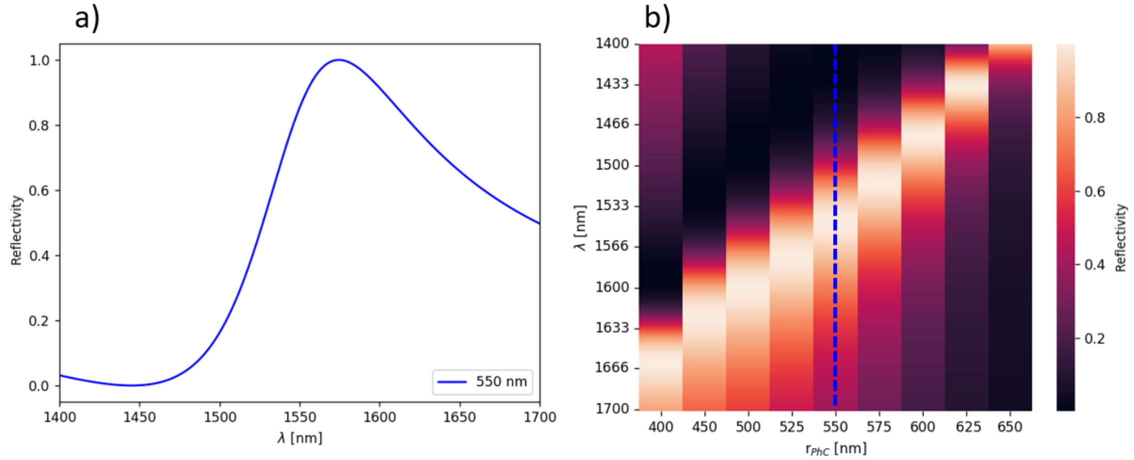

Figure 4.20: Reflectivity dependence on wavelength. a) shows the reflectivety spectra for $r_{\text{PhC}} = 550$ nm while b) shows for numerous simulations with varying r_{PhC}.

The size of the PhC, i.e. D_{Mirror} shown in Figure 2.12, is necessary to consider to minimize clipping loss. The largest waist used here for the characterization set-ups is 7.4 μm. The clipping loss for this waist calculated with Equation 2.52 is shown in Figure 4.21. It can be seen that $D_{\text{Mirror}} \geq 20\mu$m results in a optical loss which

can be neglected.

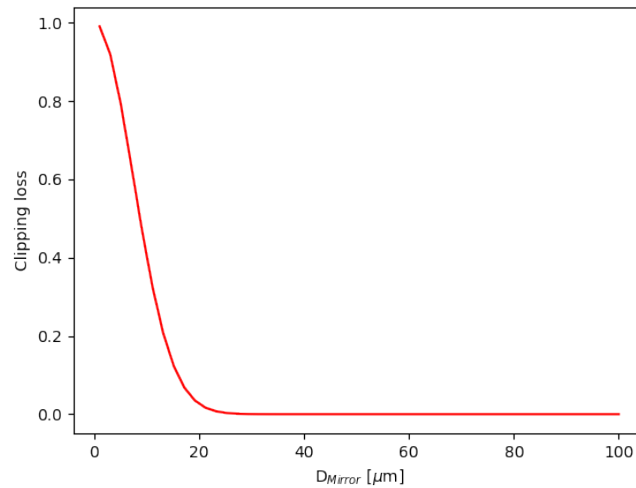

Figure 4.21: Clipping loss for different D_{Mirror} with a waist of 7.4 μm .

4.2.4 Characterization of reflectivity for PhC

Resonators with varying r_{PhC} were fabricated to verify the result from simulations. For these in total seven resonators were a a_{PhC} set to a fixed value of 1323 nm while r_{PhC} was varied between 450-600 nm. Three of these resonators are imaged with an optical microscope in Figure 4.22 together with SEM images of their PhC. Theses SEM images together with the program ProSEM were used to see if the r_{PhC} and a_{PhC} given in the mask agreed with the fabricated values. The fabricated devices' r_{PhC} showed to be 20-50 nm larger than the radius given for the mask. For a_{PhC}, no significant difference between the SEM images and the mask was observed.

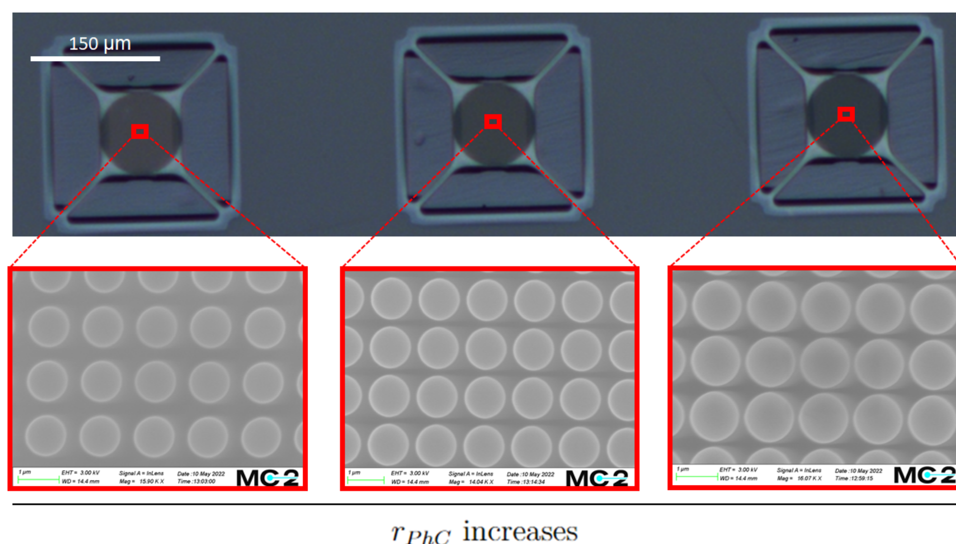

Figure 4.22: Optical and SEM images of devices with PhC with varying size of r_{PhC}.

The reflectivity was then measured for the suspended devices, and the result for a device with r_{PhC}=550 nm [1] is shown in Figure 4.23a and the compiled result from all measurements are shown in Figure 4.23b. Note that the radius reported here are the r_{PhC} given by the mask. It can here be seen that the reflectivity is high and between $40\% - 100\%$ for all wavelengths and r_{PhC}. One noticeable difference exists between the measured result in Figure 4.23 and the simulations in Figure 4.20; the measured reflectivities have two peaks. The additional peak is probably due to a guided or cavity mode that coincides at or near the reflectivity peak. The guided mode is a photonic mode inside the PhC, see Figure 4.24, and arises from a Gaussian beam. Furthermore, a cavity is created as an GaAs layer is located below the InGaP layer. The simulations made until now have not considered these additional contributions, but are included in the following simulations.

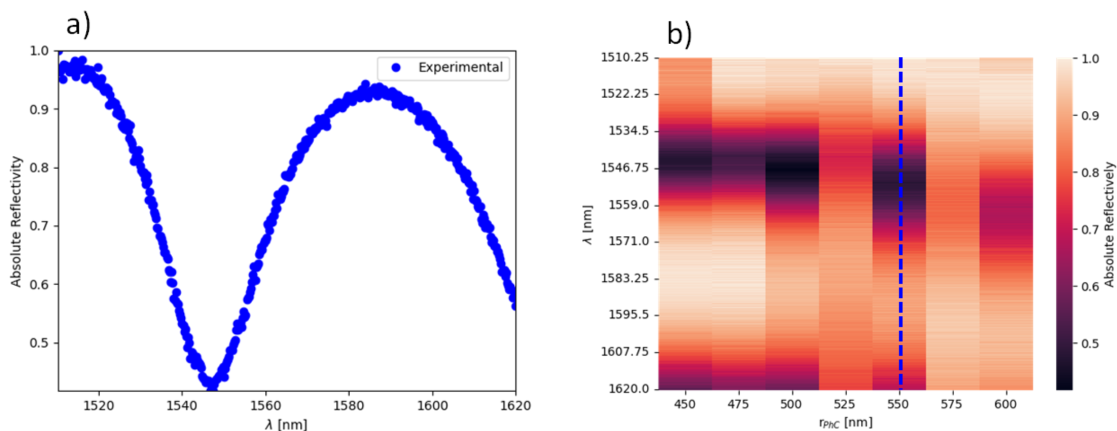

Figure 4.23: Measured reflectivity of PhC. In a) is the reflectivity for onde devices shown while multiple devices is shown in b).

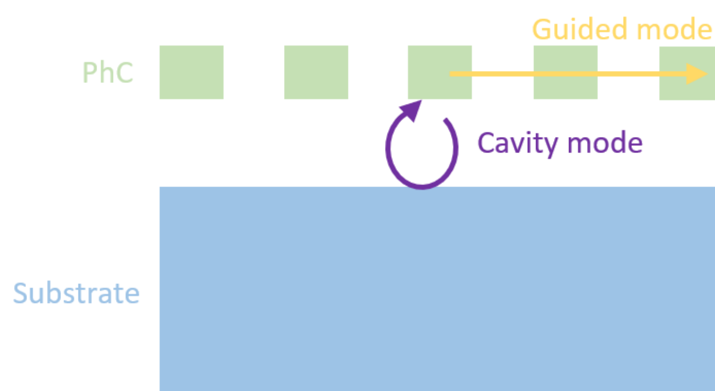

Figure 4.24: Schematic illustration of a guided and cavity mode.

The distance between the realized resonator and the substrate was measured to

[1]This is the value set for the mask. The actual measured radius was determined to be closer to 600 nm.

be $\sim 15\mu$m with a profilometer. This value was then used as a guideline for the simulations, which results are presented in Figure 4.25 [2]. The different kinds of simulations shown in Figure 4.25 were performed to see if the additional peak was due to a guided or cavity mode. The simulations presented by the orange graph consider the underlying substrate, while the green curve also considers a Gaussian beam. The simulated reflectivity which considers the underlying substrate, has multiple peaks similar to the measured data. Hence, the shape of the experimental data is due to a cavity mode. The impact the guided mode has on the simulations can be seen by comparing the green and orange curves. At a wavelength of 1520 nm, an additional dip can be seen for the green curve. However, this dip can not be seen in the experimental data. These simulations can be improved even further by using an exact refractive index of the InGaP layer.

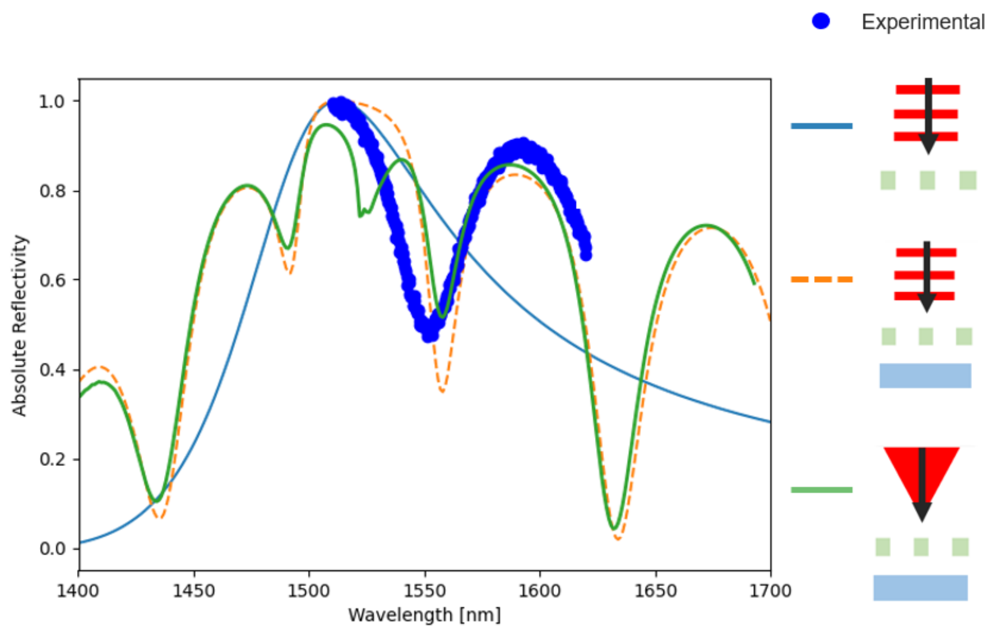

Figure 4.25: Comparison of reflectivity obtained from simulations and measurements. Three different kinds of simulations are shown here. The blue curve uses an InGaP device layer and a planar wave with an incident angle normal to the surface. The same light source is also used for the simulations presented by the green curve, but here is an underlying GaAs substrate also included. The orange curve considers the underlying substrate and uses a Gaussian beam as a light source.

[2] For the simulations shown here, the distance between the substrate and the device layer is 15.6 μm

5 Conclusion

Micromechanical resonators have many applications that require low dissipation and a high quality factor. This thesis has examine the mechanical quality factors of micromechanical resonators that were fabricated from crystalline InGaP. Further, the resonators' motion were here detected via optical means, and it was thus of interest to have a large reflectivity.

Crystalline materials have shown promising inherited properties, such as high intrinsic quality factor, inherited stress, and yield strength. The first part of this thesis investigated the first two of these. Both of which were detected by comparing fabricated strings to analytical models. A high intrinsic quality factor which varied between 5700 ± 1000 up to 7900 ± 1700 could be demonstrated. The stress was anisotropic and ranged between 200-450 MPa for suspended strings.

The next generation of resonators was trampoline-shaped, and their dimensions varied to enhance the total quality factor. This was done with simulations made in COMSOL Multiphysics to obtain a structure that resulted in minimized radiation loss, enhanced soft clamping, and strain engineering. The simulations showed that trampolines with longer and thinner tethers were more favorable for enhancing the quality factor. Soft clamping was here observed but resulted not in an enhanced quality factor for larger clamping points. Instead, smaller clamping points were more desirable due to stress engineering, which delocalized stress from the bulk to the attachment points. The trampolines with the optimized dimensions were then fabricated. The fabrications were not limited by the window and tether size but instead by the size of the diameter of the photonic crystals. A too small diameter of the photonic crystal resulted in high stress and breakage. This was taken into consideration for the next generation of trampolines and multiple of these survived. For these trampolines, the quality factor was measured for different temperatures and pressures. A quality factor as high as $7 \cdot 10^6$ was measured at low pressures and temperatures. The trampolines showed no signs of being limited by clamping loss and the geometry of the resonators. Instead, it was demonstrated that the resonators were gas damped and thus limited by the characterization set-up.

The last part of this thesis focused on the optical loss and if it could be avoided by implementing photonic crystals to the resonators. The dimensions of the photonic crystal such as its radius and lattice constant were here varied to enhance the reflectivity at a wavelength of 1550 nm. A high reflectivity at this wavelength was obtained in simulations for a lattice constant of 1323 nm and a radius of 550 nm.

These values were used as a guideline for the fabricated devices, which all showed high reflectivity but never at the desired wavelength. However, the high reflectivity was also due to cavity effects and not the design of the photonic crystal.

Future works, includes improve the mechanical characterization set-up to reach even lower pressures, to get a mechanical quality factor for the trampolines which not are limited by gas damping. Even trampolines with longer tether can be made and phononic crystals can be implemented to enhance the quality factor even further. Lastly, these types of trampolines can then be implemented in optomechanical cavities to reach the quantum regime.

Bibliography

[1] M Levinshtein, S Rumyantsev, and M Shur. *Handbook Series on Semiconductor Parameters (Vol 2) - Ternary and Quaternary III-V Compounds.* Vol. 2. 2011.

[2] Garuma Abdisa Denu, Jiao Fu, Zongchen Liu, et al. "Effect of thermoelastic damping on silicon, GaAs, diamond and SiC micromechanical resonators". In: *AIP Advances* 7.5 (2017). ISSN: 21583226. DOI: 10.1063/1.4984288.

[3] AZO Materials. *Silicon Nitride (Si3N4) Properties and Applications.* 2001. URL: https://www.azom.com/article.aspx?ArticleID=53.

[4] E. Le Bourhis and G. Patriarche. "Transmission electron microscopy observations of low-load indents in GaAs". In: *Philosophical Magazine Letters* 79.10 (1999). ISSN: 13623036. DOI: 10.1080/095008399176625.

[5] R. A. Norte, J. P. Moura, and S. Gröblacher. "Mechanical Resonators for Quantum Optomechanics Experiments at Room Temperature". In: *Physical Review Letters* 116.14 (2016). ISSN: 10797114. DOI: 10.1103/PhysRevLett.116.147202.

[6] Umesh Bhaskar, Vikram Passi, Samer Houri, et al. "On-chip tensile testing of nanoscale silicon free-standing beams". In: *Journal of Materials Research* 27.3 (2012). ISSN: 08842914. DOI: 10.1557/jmr.2011.340.

[7] Leo Sementilli, Erick Romero, and Warwick P. Bowen. *Nanomechanical Dissipation and Strain Engineering.* Jan. 2022. DOI: 10.1002/adfm.202105247.

[8] M. S. Hanay, S. Kelber, A. K. Naik, et al. "Single-protein nanomechanical mass spectrometry in real time". In: *Nature Nanotechnology* 7.9 (2012). ISSN: 17483395. DOI: 10.1038/nnano.2012.119.

[9] G. Gruber, C. Urgell, A. Tavernarakis, et al. "Mass Sensing for the Advanced Fabrication of Nanomechanical Resonators". In: *Nano Letters* 19.10 (2019). ISSN: 15306992. DOI: 10.1021/acs.nanolett.9b02351.

[10] J. Chaste, A. Eichler, J. Moser, et al. "A nanomechanical mass sensor with yoctogram resolution". In: *Nature Nanotechnology* 7.5 (2012). ISSN: 17483395. DOI: 10.1038/nnano.2012.42.

[11] Luca Leoncino. *Optomechanical transduction applied to NEMS devices.* Tech. rep. URL: https://tel.archives-ouvertes.fr/tel-01757058.

[12] Simon Gröblacher. "Quantum Opto-Mechanics with Micromirrors: Combining Nano-Mechanics with Quantum Optics". In: *Springer Theses: Recongnizing Outstanding Ph.D. Research* (2012). ISSN: 1098-6596.

[13] Silvan Schmid, Luis Guillermo Villanueva, and Michael Lee Roukes. *Fundamentals of nanomechanical resonators.* 2016. DOI: 10.1007/978-3-319-28691-4.

[14] Jean Michel Lourtioz. *Photonic crystals and metamaterials*. 2008. DOI: 10.1016/j.crhy.2007.10.006.

[15] Markus Aspelmeyer, Tobias J. Kippenberg, and Florian Marquardt. "Cavity optomechanics". In: *Reviews of Modern Physics* 86.4 (Dec. 2014), pp. 1391–1452. ISSN: 15390756. DOI: 10.1103/RevModPhys.86.1391.

[16] Pedram Sadeghi, Manuel Tanzer, Simon L. Christensen, et al. "Influence of clamp-widening on the quality factor of nanomechanical silicon nitride resonators". In: *Journal of Applied Physics* 126.16 (2019). ISSN: 10897550. DOI: 10.1063/1.5111712.

[17] Dustin W. Carr, S. Evoy, L. Sekaric, et al. "Measurement of mechanical resonance and losses in nanometer scale silicon wires". In: *Applied Physics Letters* 75.7 (1999). ISSN: 00036951. DOI: 10.1063/1.124554.

[18] Alberto Beccari, Diego A. Visani, Sergey A. Fedorov, et al. "Strained crystalline nanomechanical resonators with ultralow dissipation". In: (July 2021). URL: http://arxiv.org/abs/2107.02124.

[19] Leo Sementilli, Erick Romero, and Warwick P. Bowen. "Nanomechanical Dissipation and Strain Engineering". In: *Advanced Functional Materials* (2021). ISSN: 16163028. DOI: 10.1002/adfm.202105247.

[20] J. D. Thompson, B. M. Zwickl, A. M. Jayich, et al. "Strong dispersive coupling of a high-finesse cavity to a micromechanical membrane". In: *Nature* 452.7183 (2008). ISSN: 14764687. DOI: 10.1038/nature06715.

[21] Christoph Reinhardt, Tina Müller, Alexandre Bourassa, et al. "Ultralow-noise SiN trampoline resonators for sensing and optomechanics". In: *Physical Review X* 6.2 (2016). ISSN: 21603308. DOI: 10.1103/PhysRevX.6.021001.

[22] Alberto Beccari, Mohammad J. Bereyhi, Robin Groth, et al. "Hierarchical tensile structures with ultralow mechanical dissipation". In: (Mar. 2021). URL: http://arxiv.org/abs/2103.09785.

[23] Sabih I. Hayek. "Mechanical Vibration and Damping". In: *digital Encyclopedia of Applied Physics*. 2003. DOI: 10.1002/3527600434.eap231.

[24] O. Arcizet, P. F. Cohadon, T. Briant, et al. "Radiation-pressure cooling and optomechanical instability of a micromirror". In: *Nature* 444.7115 (2006). ISSN: 14764687. DOI: 10.1038/nature05244.

[25] Mark F. Bocko and Roberto Onofrio. "On the measurement of a weak classical force coupled to a harmonic oscillator: Experimental progress". In: *Reviews of Modern Physics* 68.3 (1996). ISSN: 00346861. DOI: 10.1103/RevModPhys.68.755.

[26] Seth B. Cataño-Lopez, Jordy G. Santiago-Condori, Keiichi Edamatsu, et al. "High- Q Milligram-Scale Monolithic Pendulum for Quantum-Limited Gravity Measurements". In: *Physical Review Letters* 124.22 (2020). ISSN: 10797114. DOI: 10.1103/PhysRevLett.124.221102.

[27] Maximilian Bückle. "Nanomechanical Systems Based on Tensile-Stressed Crystalline Indium Gallium Phosphide". PhD thesis. 2020. URL: http://nbn-resolving.de/urn:nbn:de:bsz:352-2-18flwdlcddv619.

[28] Erick Romero Sánchez. *Phononics: Engineering and control of acoustic fields on a chip*. Tech. rep. 1968.

[29] Matthias Imboden and Pritiraj Mohanty. *Dissipation in nanoelectromechanical systems.* 2014. DOI: 10.1016/j.physrep.2013.09.003.

[30] Philip S. Waggoner, Christine P. Tan, Leon Bellan, et al. “High- Q, in-plane modes of nanomechanical resonators operated in air”. In: *Journal of Applied Physics* 105.9 (2009). ISSN: 00218979. DOI: 10.1063/1.3123767.

[31] Daining FANG, Yuxin SUN, and Ai Kah SOH. “Advances in Thermoelastic Damping in Micro- and Nano- Mechanical Resonators: a Review”. In: *Journal of Solid Mechanics and Materials Engineering* 1.1 (2007), pp. 18–34. DOI: 10.1299/jmmp.1.18.

[32] H. Matsuo Kagaya and T. Soma. “Mode Grüneisen parameters and thermal expansion of GaP and InP”. In: *Solid State Communications* 58.7 (1986). ISSN: 00381098. DOI: 10.1016/0038-1098(86)90037-2.

[33] Guolong Li, Zhongzhou Ren, and Xin Zhang. “Dissipation induced by phonon elastic scattering in crystals”. In: *Scientific Reports* 6 (Sept. 2016). ISSN: 20452322. DOI: 10.1038/srep34148.

[34] Michael James Martin, Brian H. Houston, Jeffrey W. Baldwin, et al. “Damping models for microcantilevers, bridges, and torsional resonators in the free-molecular-flow regime”. In: *Journal of Microelectromechanical Systems* 17.2 (2008). ISSN: 10577157. DOI: 10.1109/JMEMS.2008.916321.

[35] RG Christian. “The theory of oscillating-vane vacuum gauges”. In: *Vacuum* 16.4 (1966). ISSN: 0042207X. DOI: 10.1016/0042-207X(66)91162-6.

[36] Minhang Bao, Heng Yang, Hao Yin, et al. “Energy transfer model for squeeze-film air damping in low vacuum”. In: *Journal of Micromechanics and Microengineering* 12.3 (2002). ISSN: 09601317. DOI: 10.1088/0960-1317/12/3/322.

[37] Bingqian Li, Haoyang Wu, Changchun Zhu, et al. “Theoretical analysis on damping characteristics of resonant microbeam in vacuum”. In: *Sensors and Actuators, A: Physical* 77.3 (1999). ISSN: 09244247. DOI: 10.1016/S0924-4247(99)00072-2.

[38] P. L. Yu, K. Cicak, N. S. Kampel, et al. “A phononic bandgap shield for high-Q membrane microresonators”. In: *Applied Physics Letters* 104.2 (2014). ISSN: 00036951. DOI: 10.1063/1.4862031.

[39] Igor A. Sukhoivanov and Igor V. Guryev. *Photonic crystals, Physics and practical modeling.* Vol. 152. 2009.

[40] Maximilian Bückle, Valentin C. Hauber, Garrett D. Cole, et al. “Stress control of tensile-strained In1-xGaxP nanomechanical string resonators”. In: *Applied Physics Letters* 113.20 (2018). ISSN: 00036951. DOI: 10.1063/1.5054076.

[41] Erick Romero, Victor M. Valenzuela, Atieh R. Kermany, et al. “Engineering the Dissipation of Crystalline Micromechanical Resonators”. In: *Physical Review Applied* 13.4 (2020). ISSN: 23317019. DOI: 10.1103/PhysRevApplied.13.044007.

[42] Y. Tsaturyan, A. Barg, E. S. Polzik, et al. “Ultracoherent nanomechanical resonators via soft clamping and dissipation dilution”. In: *Nature Nanotechnology* 12.8 (2017). ISSN: 17483395. DOI: 10.1038/nnano.2017.101.

[43] R. A. Minamisawa, M. J. Süess, R. Spolenak, et al. “Top-down fabricated silicon nanowires under tensile elastic strain up to 4.5%”. In: *Nature Communications* 3 (2012). ISSN: 20411723. DOI: 10.1038/ncomms2102.

[44] A. H. Ghadimi, S. A. Fedorov, N. J. Engelsen, et al. "Elastic strain engineering for ultralow mechanical dissipation". In: *Science* 360.6390 (2018). ISSN: 10959203. DOI: 10.1126/science.aar6939.

[45] *OPTICAL HOMODYNE DETECTION AND APPLICATIONS IN QUANTUM CRYPTOGRAPHY*. Tech. rep. 2009.

[46] Tsan-Wen Lu, Liang-Chih Wang, Cheng-Han Lai, et al. "Strain shapes the light in a photonic crystal nanocavity". In: *Photonics Research* 8.1 (2020). ISSN: 2327-9125. DOI: 10.1364/prj.8.000024.

[47] Sushanth Kini Manjeshwar, Karim Elkhouly, Jamie M. Fitzgerald, et al. "Suspended photonic crystal membranes in AlGaAs heterostructures for integrated multi-element optomechanics". In: *Applied Physics Letters* 116.26 (2020). ISSN: 00036951. DOI: 10.1063/5.0012667.

[48] Weidong Zhou, Deyin Zhao, Yi Chen Shuai, et al. *Progress in 2D photonic crystal Fano resonance photonics*. 2014. DOI: 10.1016/j.pquantelec.2014.01.001.

[49] D. Hunger, T. Steinmetz, Y. Colombe, et al. "A fiber Fabry-Perot cavity with high finesse". In: *New Journal of Physics* 12 (2010). ISSN: 13672630. DOI: 10.1088/1367-2630/12/6/065038.

[50] COMSOL multiphysics. *The Finite Element Method (FEM)*. 2017. URL: https://www.comsol.com/multiphysics/finite-element-method.

[51] Walter Frei. *Meshing Your Geometry: When to Use the Various Element Types*. 2013. URL: https://www.comsol.com/blogs/meshing-your-geometry-various-element-types/.

[52] COMSOL multiphysics. *Eigenfrequency Analysis*. 2018. URL: https://www.comsol.com/multiphysics/eigenfrequency-analysis.

[53] COMSOL multiphysics. *Perfectly Matched Layers (PMLs)*. URL: https://doc.comsol.com/5.5/doc/com.comsol.help.aco/aco_ug_pressure.05.106.html.

[54] Victor Liu. *Introduction to S4*. 2018. URL: https://web.stanford.edu/group/fan/S4/.

[55] Jari Turunen and Jani Tervo. "Fourier modal method and its applications to inverse diffraction, near-field imaging, and nonlinear optics". In: *Fringe 2013 - 7th International Workshop on Advanced Optical Imaging and Metrology*. 2014. DOI: 10.1007/978-3-642-36359-7{_}3.

[56] Victor Liu and Shanhui Fan. "S 4: A free electromagnetic solver for layered periodic structures". In: *Computer Physics Communications* 183.10 (2012). ISSN: 00104655. DOI: 10.1016/j.cpc.2012.04.026.

[57] João P. Moura, Richard A. Norte, Jingkun Guo, et al. "Centimeter-scale suspended photonic crystal mirrors". In: *Optics Express* 26.2 (2018). ISSN: 10944087. DOI: 10.1364/oe.26.001895.

[58] C. Juang. "Selective etching of GaAs and Al0.30Ga0.70As with citric acid/hydrogen peroxide solutions". In: *Journal of Vacuum Science & Technology B: Microelectronics and Nanometer Structures* 8.5 (1990). ISSN: 0734211X. DOI: 10.1116/1.584928.

[59] Michael a. Nielsen and Isaac L. Chuang. *Quantum Computation and Quantum Information: 10th Anniversary Edition*. 2011. DOI: 10.1017/CBO9780511976667.

[60] Mohammad J. Bereyhi, Alberto Beccari, Sergey A. Fedorov, et al. "Clamp-Tapering Increases the Quality Factor of Stressed Nanobeams". In: *Nano Letters* 19.4 (2019). ISSN: 15306992. DOI: 10.1021/acs.nanolett.8b04942.

A

Appendix

A.1 Data for simulations

All simulations made in this thesis is based on system shown in Figure 3.1 which consists of an InGaP and a GaAs layer. The optical and mechanical properties used for these simulations are presented here.

For the mechanical simulations, the material properties for GaAs were taken from COMSOL Library while the most of the data for InGaP was taken from the reference [27], [40] and [1]. The data taken from these works are:

Stiffness matrix [40]

$$C(x) = \begin{pmatrix} c_{11}(x) & c_{12}(x) & c_{12}(x) & 00 & 0 & 0 \\ c_{12}(x) & c_{11}(x) & c_{12}(x) & 00 & 0 & 0 \\ c_{12}(x) & c_{12}(x) & c_{11}(x) & 00 & 0 & 0 \\ 0 & 0 & 0 & c_{44}(x) & 0 & 0 \\ 0 & 0 & 0 & 0 & c_{44}(x) & 0 \\ 0 & 0 & 0 & 0 & c_{44}(x) & 0 \end{pmatrix} \tag{A.1}$$

Poisson ratio [1]

$$\nu = \frac{c_{12}}{c_{11} + c_{12}} \tag{A.2}$$

Elastic constants [1] $c_{12} = (5.61 + 0.59x) * 10^{11}$ dyn/cm^2

$c_{11} = (10.11 + 3.94x) * 10^{11}$ dyn/cm^2

$c_{44} = (4.56 + 2.47x) * 10^{11}$ dyn/cm^2

Acoustic velocity [1] 2500-5000 [1] m/s

[1]Direction dependant but is here approximated to be 4000 m/s in all directions.